ELSEVIER

Contents lists available at ScienceDirect

# Construction and Building Materials

journal homepage: www.elsevier.com/locate/conbuildmat





# Automated design of architectured polymer-concrete composites with high specific flexural strength and toughness using sequential learning

Rojyar Barhemat<sup>a</sup>, Soroush Mahjoubi a,b, Weina Meng<sup>a</sup>, Yi Bao<sup>a,\*</sup>

- a Department of Civil, Environmental and Ocean Engineering, Stevens Institute of Technology, Hoboken, NJ 07030, USA
- <sup>b</sup> Department of Materials Science and Engineering, Massachusetts Institute of Technology, Cambridge, MA 02139, USA

#### ARTICLE INFO

# Keywords: AI-assisted design of materials Architectured polymer-concrete composite (APCC) High strength and high toughness material Latin hypercube sampling Lion pride optimization Sequential surrogate modeling

#### ABSTRACT

Architectured polymer-concrete composite (APCC) is a promising structural material with high mechanical performance while optimizing the design of APCC for a high flexural strength, high toughness, and light weight remains a challenge. This paper presents a machine learning-based approach to design APCC with high specific flexural strength and toughness. The proposed approach integrates sequential surrogate modelling, Latin hypercube sampling, and Lion Pride Optimization to predict and optimize the flexural properties of APCC. The proposed approach was implemented into designing APCC beams, which were fabricated via 3D printing and tested under flexural loads. Results show that the APCC beams achieved high flexural strength, high toughness, and light weight, simultaneously. The devised architecture of APCC arrested crack propagation and promoted energy dissipation. Parametric studies were performed to evaluate the effect of key design variables of APCC on flexural properties. This research advances the basic knowledge and capabilities of AI-assisted design of APCC.

#### 1. Introduction

Concrete is the most widely used structural material worldwide. The annual consumption of concrete is 30 billion tons [1]. Compared with other structural materials such as steel and wood, concrete has important advantages ranging from constructability to mechanical properties and durability. Fresh concrete is flowable and can cast desired geometries and volumes of structures, which is challenging when steel or wood is used. For example, concrete can be used to fabricate curved façade [2] and large dams [3]. Concrete has high compressive strength, high fire resistance, high availability, low cost, low thermal conductivity, and long durability. However, concrete is brittle and weak in tension, making concrete easy to crack and fail in tension/flexure.

The current methods used to enhance the tensile and flexural properties of concrete can be categorized into two types: (1) Continuous reinforcement such as bars, tendons, and meshes, which can be made using materials with high tensile properties such as steel and fiber-reinforced polymer (FRP). The most popular types of FRP utilized to reinforce concrete are carbon FRP and glass FRP [4]. Compared with steel, FRP has lower density, higher tensile strength, and higher corrosion resistance, but FRP is often brittle and ruptures suddenly, without exhibiting a large elongation before failure. (2) Discrete reinforcement

such as chopped fibers and nanofibers. Popular chopped fibers used in concrete include steel fibers [5,6] and synthetic polymer fibers [7], which are mixed into concrete to make fiber-reinforced concrete (FRC). The chopped fibers can enhance the crack resistance via a bridging effect [8]. With the use of fibers, high-performance fiber-reinforced cementitious composites have been developed, and representative examples include ultra-high-performance concrete (UHPC) and engineered cementitious composite (ECC) [9–11]. Recently, nanofibers have been utilized in concrete to supplement the use of chopped fibers. The use of nanofibers imparts reinforcement for nano- or micro-scale cracks [12].

The above two categories of reinforcing solutions have been widely applied since they are aligned with the current structural design and construction methods. In the design of beams with continuous reinforcement, longitudinal bars usually near the top and/or bottom surfaces subject to the largest stresses. Such a philosophy simplifies the design and facilitates the construction. When discrete reinforcement is used, it can be directly added during concrete mixing, without having to significantly modify the construction process. However, adding fibers to concrete often reduces the flowability [13], so effective measures should be taken to improve the workability [14]. It is essential to control the dispersion and orientation of reinforcing fibers. Uneven fiber dispersion generates weak spots that reduce the crack resistance of concrete

E-mail address: yi.bao@stevens.edu (Y. Bao).

<sup>\*</sup> Corresponding author.

[15–17]. The fiber orientation directly affects the tensile properties of concrete [18].

Recent advances in additive manufacturing have created new opportunities to develop novel solutions of reinforcing concrete for high mechanical performance. The unique capability of three-dimensional (3D) printing for manufacturing spatially-complex geometries has enlarged the design space for the use of continuous reinforcement. The spatial layout of continuous reinforcement has gone beyond 1D straight bars and 2D plane meshes as 3D lattices have been printed to fabricate architectured composites. For example, 3D printing allows for the constructing of complex auxetic lattice structures such as honeycombs, chiral lattices, and re-entrant geometries. Each design provides unique mechanical enhancements to reinforce concrete, optimizing properties such as energy absorption [19-23]. Salazar et al. [24] proposed 3D polymeric lattices fabricated using polylactic acid (PLA) or acrylonitrile butadiene styrene (ABS). The lattices were used to fabricate polymer-concrete composite which achieved strain-hardening properties and multiple cracks. Xu and Šavija [25] fabricated ABS reinforcement meshes via 3D printing and found that the use of fine meshes in concrete achieved strain-hardening properties. Recently, a few studies have been conducted to explore the auxetic properties of composites with metal lattices filled with concrete [26-28] and to develop self-healing concrete structures with vascular polymer [29]. For instance, Zhong et al. [26] demonstrated that honeycomb structures in concrete composites can significantly enhance shear resistance. Chen et al. [27] provided experimental analysis on the static and dynamic compressive behavior of UHPC reinforced with lattice components, including re-entrant, honeycomb, and triangular lattice components, revealing that auxetic lattice structures enhanced ductility and energy dissipation under varying load conditions. Zhou et al. [28] showed that using auxetic aluminum honeycombs improved the energy absorption capabilities of auxetic structures and foam concrete under quasi-static and dynamic compression.

Previous studies demonstrated that it is feasible to use 3D printed polymer reinforcement to enhance the flexural performance of concrete. When the polymer parts are properly designed, the composite can achieve strain-hardening properties [25]. In addition, the light weight and the high corrosion resistance of polymer make it promising to develop lightweight and durable structures. Another lesson learned is that the mechanical properties of polymer-concrete composite are related to the geometry and dimensions of polymer lattices [25]. To date, the effects of the design variables of polymer lattices on the mechanical properties and the influencing mechanisms are still unclear. Due to this fundamental knowledge gap, the flexural strength and toughness are limited.

To address this challenge, this research aims at developing architectured polymer-concrete composite (APCC) with high flexural strength, high toughness, and light weight. To achieve this goal, this research has three objectives: (1) to develop an optimization framework to promote the design of APCC by integrating Latin hypercube sampling (LHS) [30], sequential surrogate modeling [31], and Lion Pride Optimization Algorithm (LPOA) [32]; (2) to implement the framework into the design of APCC; and (3) to understand the fracture mechanism and investigate the effects of design variables on the flexural strength and toughness of APCC. The novelty is the development and utilization of the AI framework for designing APCC towards high flexural strength, high toughness, and light weight.

The remainder of the paper is organized as follows: Section 2 presents the methods and AI framework. Section 3 elaborates on the experimental and simulation results and underlying fracture mechanism of APCC for high flexural strength, high toughness, and light weight. Section 4 presents the optimal design of APCC; and Section 5 concludes the new findings.

# 2. Methods

The methods adopted in this paper are elaborated in four

subsections: Section 2.1 overviews the AI framework; Section 2.2 presents the design of APCC with high specific flexural properties; Section 2.3 elaborates on the manufacturing and experimental testing of APCC beams; and Section 2.4 elaborates on the finite element model and the investigated cases for the design of APCC.

#### 2.1. Overview

An AI-based design framework is presented to design APCC, aimed at achieving high specific flexural strength and toughness. The flowchart of the AI framework is shown in Fig. 1. The framework includes three steps: (1) A dataset is generated to relate the mechanical properties of APCC to the key design variables via finite element analysis [33] based on LHS [30] (Section 2.2.2). (2) The dataset is utilized to develop a sequential surrogate model [31] for predicting the flexural properties of APCC (Section 2.2.3). (3) The predictive model is integrated with LPOA [32] for determining the optimal design of APCC (Section 2.2.4), aiming to utilize the high efficiency of metaheuristic optimization [34,35]. Based on this framework, this research developed finite element models to investigate the effect of design variables on the mechanical properties of APCC and the underlying mechanisms (Section 2.4). The proposed method and finite element models were validated using experimental testing data (Section 2.3).

#### 2.2. Design method

#### 2.2.1. Initial design

The envisioned APCC is composed of architectured polymer lattices and concrete matrix, as shown in Fig. 2. The APCC is fabricated in two steps. First, a lattice structure is fabricated using a 3D printer and polymer filaments. Then, the polymer lattice is placed in a mold, and concrete is poured to cast APCC. A detailed description of the experimental testing is provided in Section 2.3.

In the initial design, the main consideration is the manufacturability: (1) It is feasible and efficient to manufacture architectured polymer lattices through 3D printing [36]. (2) The distance between voids in the architectured polymer lattices is suitable for casting concrete within the lattice structure. The voids of the architectured polymer lattices should be interconnected and large enough for fresh concrete to fill and consolidate.

An initial design and the design variables are shown in Fig. 3. The design variables include: (1) the spacings between adjacent filaments, designed by  $d_x$ ,  $d_y$ , and  $d_z$ , which are the spacing between adjacent filaments along X, Y, and Z; and (2) the sizes of filaments, designed by  $v_x$ ,  $v_y$ , and  $v_z$ , which are the width of each filament along X, Y, and Z. In the initial design, the spacing between adjacent filaments ( $d_x$ ,  $d_y$ , and  $d_z$ ) is 15 mm along X, Y, and Z; and the width of each filament ( $v_x$ ,  $v_y$ , and  $v_z$ ) is 5 mm along X, Y, and Z. The concerned properties are the specific flexural strength ( $\delta$ ) and specific toughness ( $\beta$ ), as defined in Eq. (1) and Eq. (2):

$$\delta = \frac{S}{P} \tag{1}$$

$$\beta = \frac{T}{D} \tag{2}$$

where  $\delta$  and  $\beta$  are the specific flexural strength and specific toughness of APCC, respectively; S is the flexural strength of APCC; T is the toughness of APCC, defined as the area under the load-displacement curve; and D is the density of APCC.

To assess the performance of the initial design of APCC, five APCC beam specimens were fabricated and tested under four-point bending until failure, as elaborated in Section 2.3. The experimental results were then compared with the finite element analysis results obtained, as elaborated in Section 3.

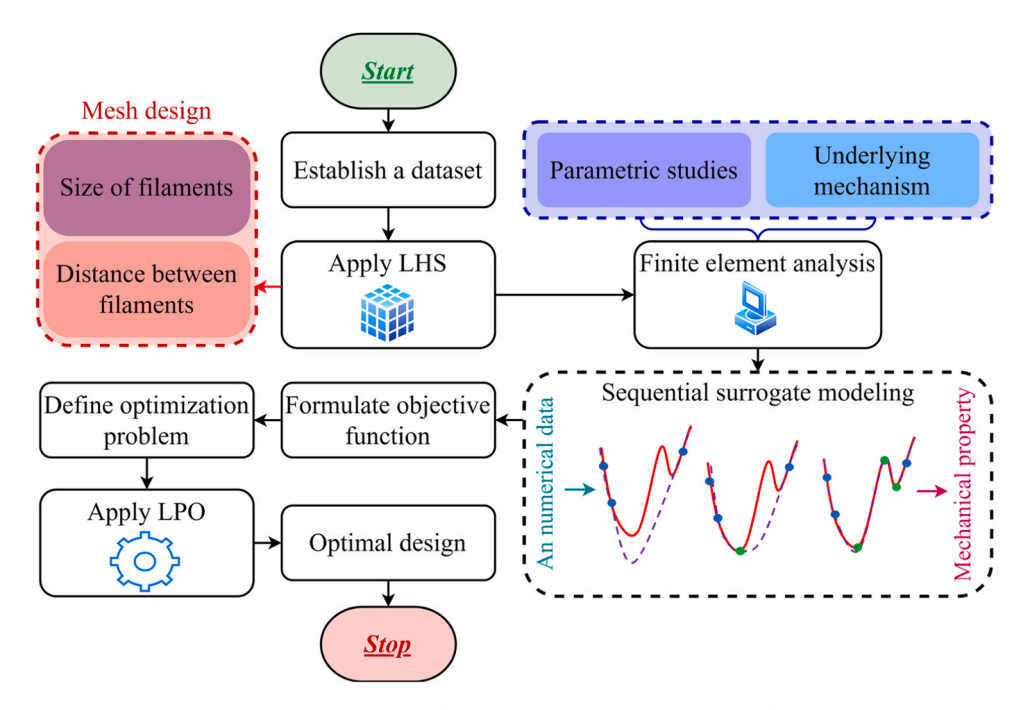


Fig. 1. Flowchart of the proposed AI-assisted material design framework for APCC.

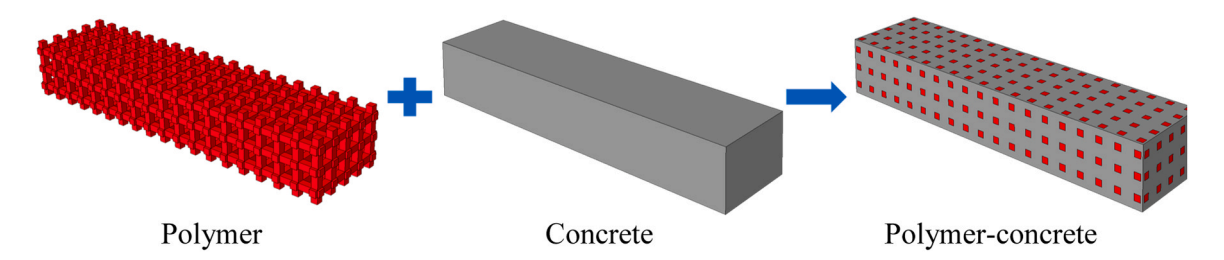


Fig. 2. Main structure of the APCC composed of architectured polymer lattices and concrete.

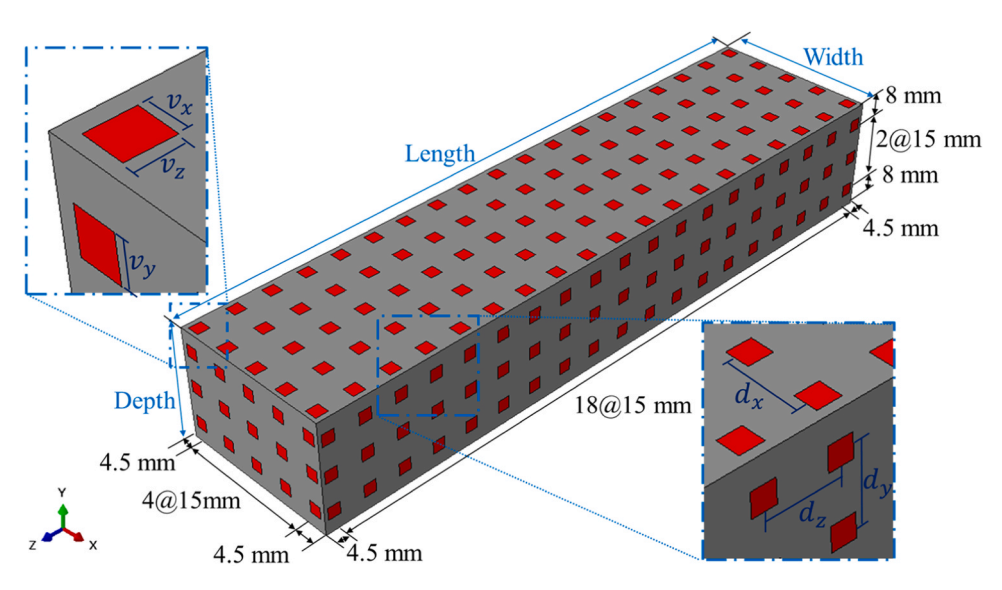


Fig. 3. Initial design and definition of the design variables of APCC scalable for large structures.

# 2.2.2. Establishment of dataset

To optimize the design of APCC, it is necessary to establish a dataset of various designs of APCC and the corresponding flexural properties. In this research, finite element analysis was conducted using a commercial

software, namely ABAQUS [33], to establish the dataset. The finite element model and model validation are elaborated in Section 2.4 and Section 3, respectively. The design variables of APCC were utilized as the input variables. The flexural properties of APCC were the output

variables. The input variables were sampled using the LHS method [30], a statistical technique that divides the range of each parameter into equal intervals. By sampling each interval exactly once, LHS ensures a uniformly distributed sample set across all parameters. Previous research showed that the LHS method was effective in reducing the number of sampling points [37] and recommended that the number of initial samples should be 10 times the number of design variables [38]. In this research, with six design variables considered, the number of initial finite element models was set at 60. With the sampled input variables of APCC, the flexural properties of APCC were determined through finite element analysis. After the dataset was generated, it was split into a training set and a test set.

#### 2.2.3. Sequential surrogate model

This study developed a sequential surrogate model to approximate the behavior of complex systems [31]. Sequential surrogate models, a type of machine learning technique, are utilized when systems are computationally intensive, particularly in complex simulations like 3D nonlinear finite element analysis (FEA) that incorporate nonlinear material properties and damage. These factors can make FEA models challenging to converge, requiring significant computational resources. A sequential surrogate model can be constructed through various machine learning techniques, including radial basis function models [39], Kriging models [40], and artificial neural networks [41]. In this study, a Kriging model is utilized as a surrogate model to predict the flexural properties of APCC. In the operation of the sequential surrogate model, new sampling points are iteratively added to the training set based on a sequential sampling technique. This process is recognized as an active learning/training process, which allows the sequential surrogate model to improve when more data becomes available [42]. The concept of sequential surrogate models is shown in Fig. 4. The methods of Expected Improvement (EI) [43,44] and Mean Square Error (MSE) [45] were used to establish the standards for selecting more samples that are used to enlarge the training set and enhance the efficiency of sequential surrogate models. More details about infill criteria for expanding the training set are elaborated in Section 2.2.3.2.

The flowchart for establishing the sequential surrogate model is shown in Fig. 5. There are five main steps [46]: (1) Establish the training and test datasets (Section 2.2.2). (2) Train the surrogate model using the training dataset (Section 2.2.3). (3) Test the performance of the trained predictive model using the test dataset unseen in the training process. Two performance metrics, the coefficient of determination ( $R^2$ ) and root mean square error (RMSE), are employed to assess the accuracy of the surrogate model (Section 2.2.3.1). (4) Improve the performance of the trained surrogate model by adding more samples to the training dataset using two infill criteria, namely EI and MSE (Section 2.2.3.2). (5) Repeat Steps 3–5 until the stopping criteria are met. Two stopping criteria are defined in Section 2.2.3.2.

#### 2.2.3.1. Performance metrics. Two performance metrics were utilized,

which are  $\mathbb{R}^2$  and  $\mathbb{R}MSE$ , which are defined in Eq. (3) and Eq. (4), respectively.

$$R^{2}(X,Y) = 1 - \frac{\sum_{i=1}^{n} (x_{i} - y_{i})^{2}}{\sum_{i=1}^{n} [y_{i} - mean(y_{i})]^{2}}$$
(3)

$$RMSE(X,Y) = \sqrt{\frac{\sum_{i=1}^{n} (x_i - y_i)^2}{n}}$$
(4)

where  $X = \{x_1, x_2, ..., x_n\}$  denote the predicted values;  $Y = \{y_1, y_2, ..., y_n\}$  denote the actual values; and n denotes the number of observed data points.

2.2.3.2. Stopping and infill criteria. The stopping criterion determines when the training process is terminated. Two specific stopping criteria shown in Eq. (5) and Eq. (6) are utilized:

$$R_i^2 \ge R_{Thresh}^2 \tag{5}$$

$$|RMSE_i - RMSE_{i+1}| \le \Delta RMSE_{Thresh}(1 + |RMSE_i|)$$
 (6)

where subscript i is the number of infill samples, and subscript *Thresh* is the threshold of the stopping criteria. To ensure the predictive model have high accuracy and generalizability,  $R_{Thresh}^2$  and  $\Delta RMSE_{Thresh}$  are set at 0.91 and  $0.06 \times 10^6$  kN·mm<sup>3</sup>/kg, respectively.

To improve the accuracy of the surrogate predictive model, in the training process, more samples were added to the training dataset before the stopping criteria were met. Two infill criteria were applied: When  $R^2$  is below 0.9, new samples are added using *MSE*, as defined in Eq. (7). When  $R^2$  is greater than or equal to 0.9, new samples are added using *EI* (Eq. (8)).

$$\widehat{S}^{2}(y(x^{*})) = \sigma^{2}(1 - t^{\varphi}\varphi^{-1}t)$$
(7)

$$EI(x) = \frac{y_{\min} - \hat{y}(x^*)}{2} \left[1 + erf(\frac{y_{\min} - \hat{y}(x^*)}{\sqrt{2}\hat{S}^2[y(x^*)]})\right] + \frac{\hat{S}^2[y(x^*)]}{\sqrt{2\pi}} \exp\left[\frac{\hat{y}(x^*) - y_{\min}}{2\hat{S}^2[y(x^*)]}\right]$$
(8)

where  $\sigma^2$  is the dispersion in the mean of the predictive model;  $\varphi$  is the correlation matrix between two given input variables; t is the correlation between a newly added sample and the existing samples in the training dataset;  $y_{\min}$  is the current optimal value; erf is the error function;  $y(x^*)$  is the predicted value of the new sample;  $\widehat{y}(x^*)$  and  $\widehat{S}^2[y(x^*)]$  are the mean and variance of the random Gaussian process, respectively.

#### 2.2.4. Optimization method

Lion Pride Optimization Algorithm (LPOA) which is a nature-inspired metaheuristic algorithm [32] was utilized to perform

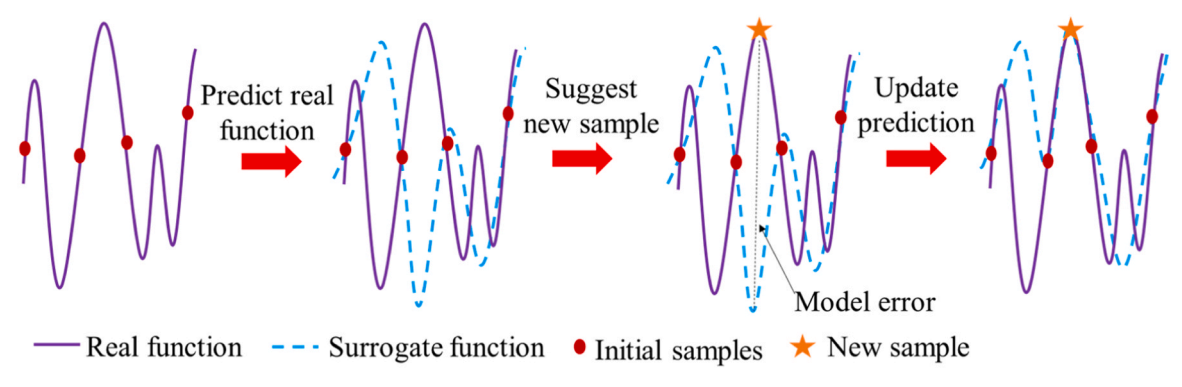


Fig. 4. Concept of the sequential surrogate modeling technique employed to design APCC.

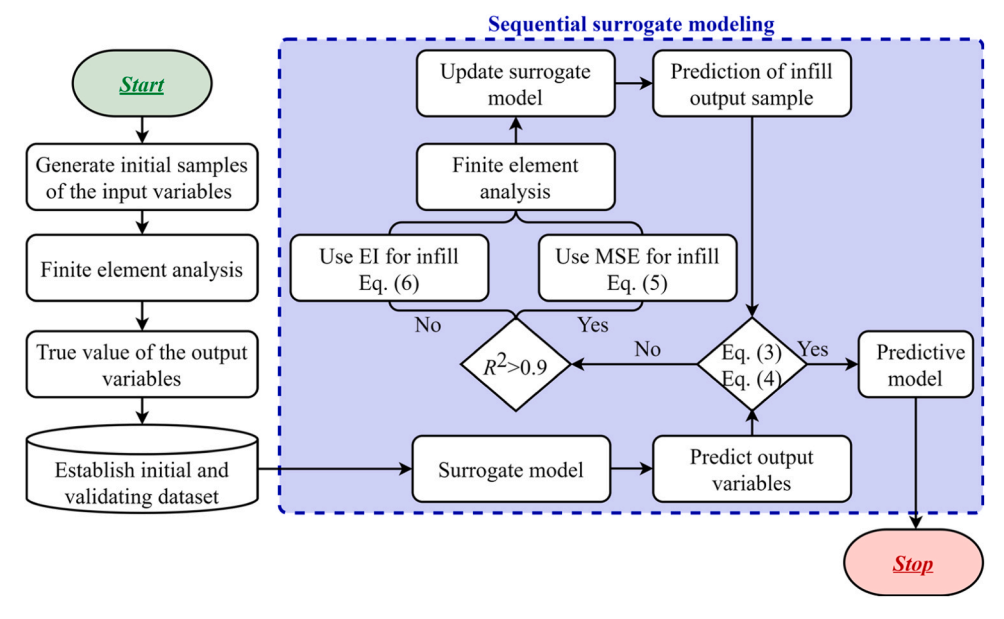


Fig. 5. Process of the sequential surrogate modelling for predicting and optimizing APCC.

optimization to obtain the optimal design of APCC. The LPOA has been detailed in reference [32], so its introduction is not repeated in this study. The number of generations and population size were set to 300 and 100, respectively.

The design of APCC was formulated as an optimization problem that aims to maximize the specific flexural strength and the specific toughness. Table 1 lists six design variables and their ranges. The ranges were determined based on the highest values of the specific flexural strength and the specific toughness in a parametric study while considering manufacturability (Section 3.1).

In the optimization process, to ensure an appropriate consolidation of concrete, a design constraint was imposed to enforce that the empty spacings between adjacent polymer filaments are not less than 3 mm, which is considered sufficiently large to fill with the mortar. A penalty function approach was adopted to transform the constrained optimization problem into an unconstrained optimization problem. A penalized objective function  $F_{Penalty}$  is defined as the product of the original objective function F and a penalty function  $F_{Penalty}$ .

$$F_{Penalty} = F \times f_{penalty} \tag{9}$$

$$f_{penalty} = \left[1 + \gamma_1 \times (\omega_x + \omega_y + \omega_z)\right]^{\gamma_2} \tag{10}$$

$$\omega_i = \begin{cases} \sum_{i=1}^{n} (1 - \frac{d_{i\max}}{d_i}) & if \omega_i > d_{i\max} \\ 0 & if \omega_i < d_{i\max} \end{cases}$$
(11)

where  $d_i$  is the spacing between adjacent filaments;  $d_{i\max}$  is the upper boundary value constraint for the variable  $d_i$ ;  $\gamma_1$  and  $\gamma_2$  are two constants; and  $\omega_i = \left\{ \omega_x, \ \omega_y, \ \omega_z \right\}$  is the extent of violation of design limits. In this study,  $\gamma_1$  was fixed at 1.0, and  $\gamma_2$  gradually increased from 1.3 to

**Table 1**Ranges of the design variables.

Number	Design variables	Range (mm)
1	$\nu_x$	1–12
2	$ u_{\mathrm{y}}$	1–12
3	$ u_z$	1–12
4	$d_x$	10-40
5	$d_{y}$	10-40
6	$d_z$	10–40

3.0 in the optimization process, following the approach described in reference [47].

#### 2.3. Experiments

For the flexural tests, seven APCC beams were fabricated: five beams with the initial design and two beams with the optimal design. A larger number of samples for the initial design was used to develop high-fidelity finite element models, critical for accurately predicting and optimizing the APCC beams. With the validated models, two samples for the optimal design were fabricated and tested, and the test results of the two samples were consistent with the results from the finite element model. The optimization method for determining the optimal design is detailed in Section 2.2, with further optimization information provided in Section 4.

The beam specimens were fabricated in two steps. First, architectured ABS lattices were printed through fused deposition modeling (FDM) [48] using a commercial 3D printer (model: Flashforge Guider II). Computer models of ABS lattices were created as stereolithography (STL) files, which were utilized to produce ABS lattices layer by layer, as shown in Fig. 6.

The ABS filament was heated to a semi-molten state, characterized by reduced viscosity and increased molecular mobility. This condition allows the filament to be extruded through the nozzle and deposited in layers to form the desired 3D object. The parameters used in the 3D

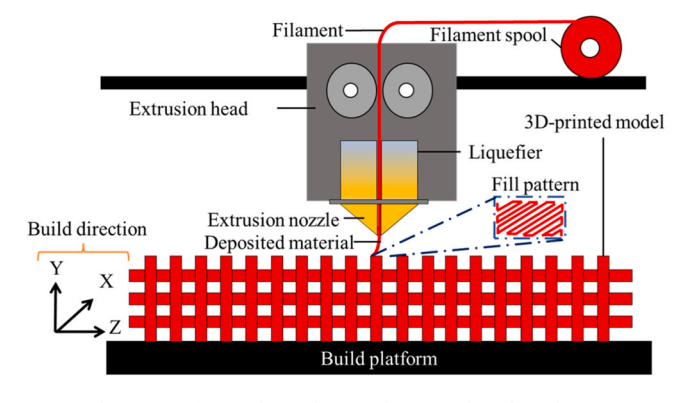


**Fig. 6.** Fabrication of 3D polymer lattices for APCC based on the 3D printing through FDM.

printing process are listed in Table 2. The density and the Poisson's ratio of ABS are  $792 \text{ kg/m}^3$  and 0.35, respectively. In this study, ABS was adopted to develop the method. With the method, other types of polymers can be utilized in future investigations and applications.

The polymer lattices were placed in beam molds, followed by casting concrete. Each mold measured 76 mm  $\times$  50 mm  $\times$  300 mm and was oiled before the placement of polymer lattices. The concrete represents a typical construction mortar. The formulation is listed in Table 3. The water-to-binder ratio was 0.45. The binder was composed of Type I Portland cement and slag sourced from a local supplier in New Jersey, USA. The chemical compositions and physical characteristics of Portland cement, slag, and river sand are listed in Table 4. To improve the flowability, a high-range water reducer was used. The mini-slump spread was 300 mm, which is sufficient to achieve self-consolidation without having to apply external vibration. The compressive strength of concrete was evaluated using cubic specimens (50 mm  $\times$  50 mm  $\times$ 50 mm) according to ASTM 109 C [49]. Each test was replicated three times. The compressive strength was evaluated at 7 days, which aligns with the assessment of early-age behavior of APCC for applications that require high early-age strengths, consistent with references [24,25]. The compressive strength at 7 days was 35 MPa  $\pm$  3 MPa. The density and Poisson's ratio were 2500 kg/m<sup>3</sup> and 0.2, respectively. The elastic modulus was evaluated in accordance with ACI 318 [50].

Immediately after concrete casting, the beams were covered using plastic sheets to avoid moisture loss. The beams were kept in molds for 24 hours. After the molds were removed, the beams were stored in a curing tank with a lime-saturated solution. After the beams were cured for 7 days, they were air dried for 24 hours (room temperature:  $20 \pm 2$  °C: relative humidity:  $50 \% \pm 5 \%$ ).

The beams were then tested until failure with a four-point bending test setup, as shown in Fig. 7. The beams were supported by two rollers and loaded by two other rollers that were attached to a universal load frame (model: Instron 5960). The span length was 260 mm, and the load spacing was 94 mm. The tests were conducted under a displacement control mode with a displacement rate of 1 mm/min. The deflections of the beam was monitored using displacement sensors. The loading was terminated after the carried load dropped to below 85 % of the peak load.

### 2.4. Finite element analysis

The mechanical behaviors of APCC beams were analyzed via 3D finite element analysis. The finite element model is shown in Fig. 8. The structure and boundary condition of the APCC beams are consistent with the experiments. The dimensions of polymer filaments and the spacing between adjacent polymer filaments are elaborated in Section 2.4.1. Concrete and polymer were modeled using 3D eight-node solid elements with reduced integration (C3D8R). The interaction between polymer and concrete was defined using the keyword "embed", meaning that polymer and concrete were bonded. Further discussions on the interface between polymer and concrete are provided in Section 3 based on the results.

A mesh sensitivity analysis was performed to determine the ideal

**Table 2** Parameters of 3D printing.

Printing parameter	Configuration
Filament diameter	2.85 mm
Nozzle diameter	0.4 mm
Layer thickness	0.1 mm
Maximum speed	70 mm/s
Minimum speed	5 mm/s
Temperature	240 °C
Infill density	100 %
Fill pattern	Line
Filament material	ABS

**Table 3**Mixture design of concrete.

Type I Portland cement	River sand	Water	HRWR
739.4	1244.1	295.7	3.0

**Table 4**Chemical and physical properties of the dry ingredients of concrete.

Components	Type I Portland cement	Slag	River sand
SiO <sub>2</sub> (%)	22.44	36.21	80.30
Al <sub>2</sub> O <sub>3</sub> (%)	2.76	11.10	10.50
Fe <sub>2</sub> O <sub>3</sub> (%)	2.24	0.76	3.43
CaO (%)	68.05	43.75	1.72
MgO (%)	0.91	5.09	1.70
SO <sub>3</sub> (%)	2.25	2.21	1.07
Na <sub>2</sub> O (%)	0.19	0.23	-
K <sub>2</sub> O (%)	0.11	0.40	-
TiO <sub>2</sub> (%)	0.14	0.58	-
P <sub>2</sub> O <sub>5</sub> (%)	0.09	0.02	-
$Mn_2O_3$ (%)	0.03	0.36	-
C <sub>3</sub> S (%)	62.35	-	-
C <sub>2</sub> S (%)	20.28	-	-
C <sub>3</sub> A (%)	1.42	-	-
C <sub>4</sub> AF (%)	5.83	-	-
Loss of ignition (%)	1.28	0.72	1.28
Specific gravity (g/cm <sup>3</sup> )	3.15	2.9	2.65

mesh size within a range of 3 mm to 0.5 mm, selected based on the 1 mm minimum size of the polymer filaments. The simulations showed convergence at a mesh size of 1 mm or smaller. Therefore, to maintain a balance between computational efficiency and model accuracy, a mesh size of 1 mm was chosen. Further reducing the mesh size did not greatly improve the accuracy but substantially compromised the computation efficiency which is a key factor in design optimization.

Regarding the loading method, the beams were subjected to forced displacements until the load carrying capability was reduced to 85 % of the peak load or lower. In the damage process of APCC beams, the energy dissipation behaviors of concrete and polymer were considered by investigating the energy dissipated per unit volume by plastic deformation (EPDDEN).

The constitutive relationships of concrete and ABS are shown in Fig. 9. The damages of concrete were considered using a concrete damaged plasticity (CDP) model, which was used to consider compressive and tensile damages, as shown in Fig. 9(a). CDP model parameters are listed in Table 5. More details of CDP models are available in references [51,52].

ABS was modelled as a ductile material, and the tensile properties were modelled using a multi-linear model, as shown in Fig. 9(b). The mechanical properties of ABS are listed in Table 6. The manufacturer-specified density of ABS was 1100 kg/m<sup>3</sup>.

Based on the finite element model, the effect of the variables of the polymer lattices on the flexural properties of APCC was evaluated via a parametric study, as listed in Table 7. The number of polymer filaments along X, Y, and Z directions can be computed as:

$$N = Floor\left(\frac{K - V}{D}\right) + 1 \tag{14}$$

where  $N = \{n_x, n_y, n_z \}$  is the number of polymer filaments;  $K = \{k_x, k_y, k_z\}$  is the dimension of an APCC beam;  $V = \{v_x, v_y, v_z\}$  is the polymer filament dimensions; and  $D = \{d_x, d_y, d_z\}$  is the spacing between adjacent polymer filaments.

## 3. Experimental and simulation results

The failure patterns of the five beams fabricated according to the initial design of APCC are shown in Fig. 10. The varying colors of the

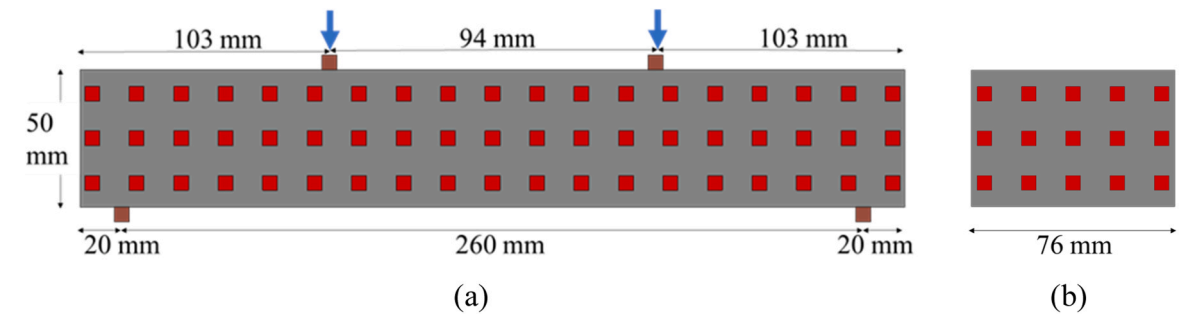


Fig. 7. Example of APCC beams under four-point bending: (a) front view, and (b) side view.

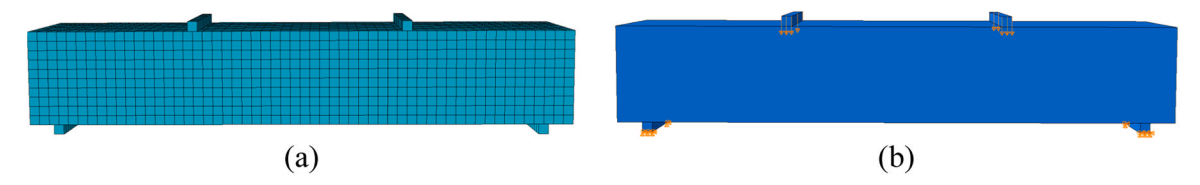


Fig. 8. Finite element model: (a) meshed model, and (b) loading and boundary conditions.

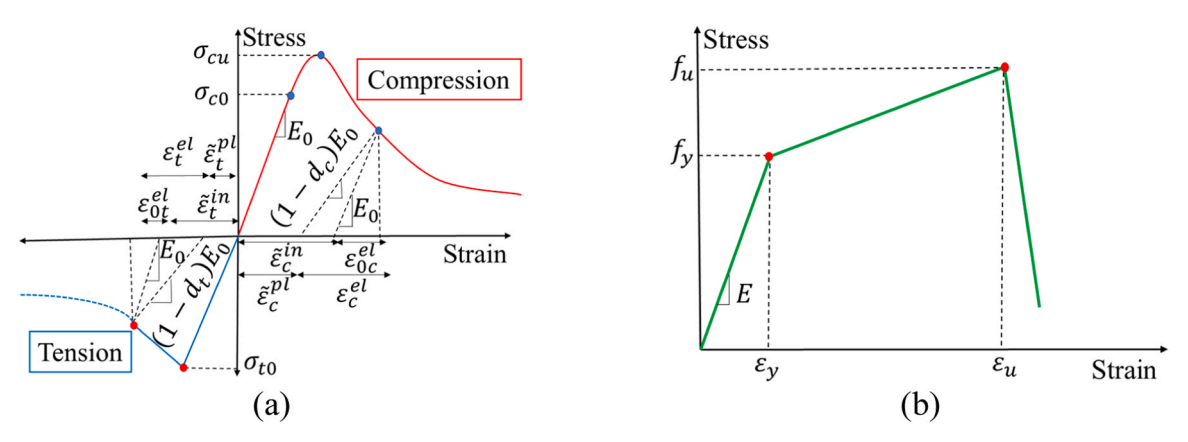


Fig. 9. Constitutive relationships of the used materials: (a) concrete [53]; and (b) ABS [54].

**Table 5**Parameters of the adopted CDP model.

Density (kg/m³)	Poisson's ratio	Young's modulus (GPa)	Dilation angle	Eccentricity	fb <sub>0</sub> /fc <sub>0</sub>	K	Viscosity parameter
2500	0.2	30	31	0.1	1.16	0.67	0

**Table 6**Mechanical properties of ABS.

Young's modulus (GPa)	Poisson's ratio	Yield strength (MPa)	Ultimate strength (MPa)	Plastic strain	Ductile damage	Ductile damage		
					Fracture strain	Stress triaxiality	Strain rate	
2.4	0.35	25.77	33.32	0.0455	0.05	0.333	0.0002	

tested specimens are attributed to the different lighting conditions and backgrounds in the laboratory where the specimens were photographed. Specifically, specimen-1 was photographed on a cream-colored surface, whereas the other specimens were placed on a glossy black surface, which influenced their perceived color in the images. Vertical flexural cracks were observed from the flexural span of each beam.

The cracks initiated from the bottom and then extend to the top of the beams with the increase of the load levels. Some horizontal cracks were observed from the middle depth of the beams. The positions of cracks were well correlated with the positions of the polymer lattices. The widths of the cracks were in the range of 20  $\mu m$  to 50  $\mu m$  when they were initiated and then increased with the increase of the applied load. The crack width is dependent on many factors such as the diameter, aspect ratio, surface roughness, and mechanical properties (e.g., elastic modulus, tensile strength, and toughness) of the reinforcement material, the mechanical properties of the host concrete, and the mechanical properties of the interface between the reinforcement and host materials.

Table 7
Investigated cases in the parametric study.

Design variables	Designation	$\nu_x$	$\nu_y$	$\nu_z$	$d_x$	$d_{y}$	$d_z$
	Initial	5	5	5	15	15	15
$\nu_x$	$\nu_x$ -1	1	5	5	15	15	15
	$v_x$ -3	3	5	5	15	15	15
	$v_x$ -7	7	5	5	15	15	15
	$v_x$ -9	9	5	5	15	15	15
$\nu_{\rm y}$	$\nu_y$ -1	5	1	5	15	15	15
	$v_y$ -3	5	3	5	15	15	15
	$v_y$ -7	5	7	5	15	15	15
	$v_y$ -9	5	9	5	15	15	15
$\nu_z$	$v_z$ -1	5	5	1	15	15	15
	$v_z$ -3	5	5	3	15	15	15
	$v_z$ -7	5	5	7	15	15	15
	$v_z$ -9	5	5	9	15	15	15
$d_x$	$d_x$ -10	5	5	5	10	15	15
	$d_{x}$ -20	5	5	5	20	15	15
	$d_{x}$ -25	5	5	5	25	15	15
	$d_x - 30$	5	5	5	30	15	15
$d_{y}$	$d_y$ -10	5	5	5	15	10	15
	$d_{y}$ -20	5	5	5	15	20	15
	$d_{y}$ - 25	5	5	5	15	25	15
	$d_{y} - 30$	5	5	5	15	30	15
$d_z$	$d_z - 10$	5	5	5	15	15	10
	$d_z$ -20	5	5	5	15	15	20
	$d_z$ -25	5	5	5	15	15	25
	$d_z - 30$	5	5	5	15	15	30

During the testing, spalling of concrete was not observed from the test APCC beams, as shown in Fig. 10. The observation suggests that while debonding occurs, it primarily affects internal stress redistribution while it does not lead to the loss of outside concrete. After the beams failed, the fracture sections were inspected. It was found that polymer lattices were embedded in concrete and ruptured at the fracture sections.

The load versus mid-span deflection curves of the five APCC beams are plotted in Fig. 11. The load first linearly increased with deflection at the beginning. After the concrete was cracked, the load continued increasing, but the load increasing rate was reduced. The load-deflection curves show that the beams achieved strain-hardening properties which can be attributed to the use of ABS lattices because concrete is brittle. With the increase of deflection, more and more cracks were generated in concrete. The generation of more cracks are reflected by the fluctuations of loads in the load-deflection curves. Finally, the beams fractured, and the load decreased to zero. The finite element analysis results are compared with the test results, and their good agreement indicates that the finite element model provided reasonable predictions of the flexural behavior of the APCC beam.

## 3.1. Parametric study results

The effect of the design variables  $v_x$ ,  $v_y$ ,  $v_z$ ,  $d_x$ ,  $d_y$ , and  $d_z$  on the flexural behavior of APCC beams is shown in Fig. 12. All APCC beams

show strain-hardening behaviors, similar to the behaviors observed from Fig. 11. The results of specific flexural strength ( $\delta$ ) and specific toughness ( $\beta$ ) of the investigated APCC beams are summarized in **Table A1** in the Appendix.

Increasing the dimensions of ABS filaments along X and Y directions  $(\nu_x$  and  $\nu_y$ ) increases  $\delta$  and  $\beta$ . Specimens  $\nu_x$ -9 and  $\nu_y$ -9 exhibit the highest  $\delta$  and  $\beta$ . Increasing the dimensions of ABS filaments along Z direction  $(\nu_z)$  increases  $\delta$ . Specimen  $\nu_z$ -9 exhibits the highest  $\delta$ . When  $\nu_z$  is less than 5 mm,  $\beta$  increases with  $\nu_z$ . However, when  $\nu_z$  is larger than 5 mm,  $\beta$  decreases with  $\nu_z$ . Specimen  $\nu_z$ -5 has the highest  $\beta$ . Overall, increasing the spacings between ABS filaments decreases  $\delta$  and  $\beta$ . Specimens  $d_x$ -10,  $d_y$ -10, and  $d_z$ -10 exhibit the highest  $\beta$ .

The results of  $\delta$  and  $\beta$  are plotted in Fig. 13. Along X direction, increasing the dimension of filaments and decreasing the spacing between polymer filaments increase  $\delta$  and  $\beta$ , as shown in Fig. 13(a) and Fig. 13(d). Along Y direction, increasing  $v_y$  and decreasing  $d_y$  increase  $\delta$  and  $\beta$ , as shown in Fig. 13(b) and Fig. 13(e). Along Z direction, increasing  $v_z$  increases  $\delta$ ; and  $\beta$  first increases and then decreases with  $v_z$ , as shown in Fig. 13(c). Decreasing the spacing between polymer filaments increases  $\delta$  and  $\beta$ , as shown in Fig. 13(f). The parametric study results suggest that  $\delta$  and  $\beta$  can be increased by increasing the polymer filament dimensions (v) along X, Y and Z directions when  $v_z$  is less than 5 mm, and decreasing the spacing between adjacent ABS filaments along X, Y and Z directions.

#### 3.2. Damage mechanisms

The damage process of the initial design of APCC beams is shown in Fig. 14. The cracks in concrete are indicated by a tension damage index (DAMAGET), which is in the range of 0 (no crack) to 1 (fully cracked).

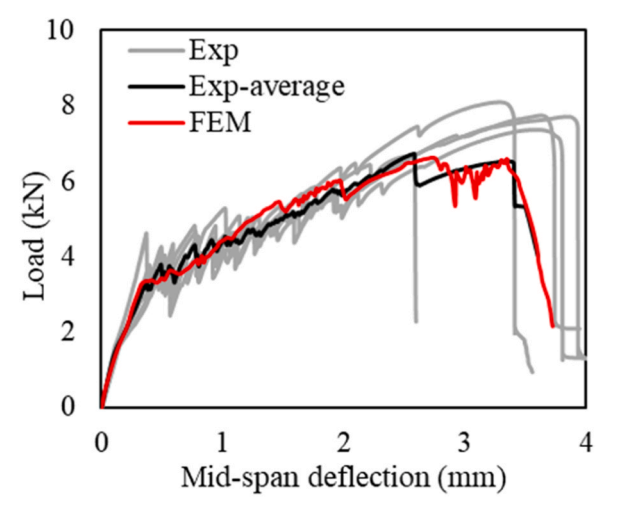


Fig. 11. Experimental (EXP) and finite element analysis (FEM) results of the APCC beams.



Fig. 10. Photos of damaged APCC specimens showing the distribution of cracks and fractured section of the initial design of APCC.

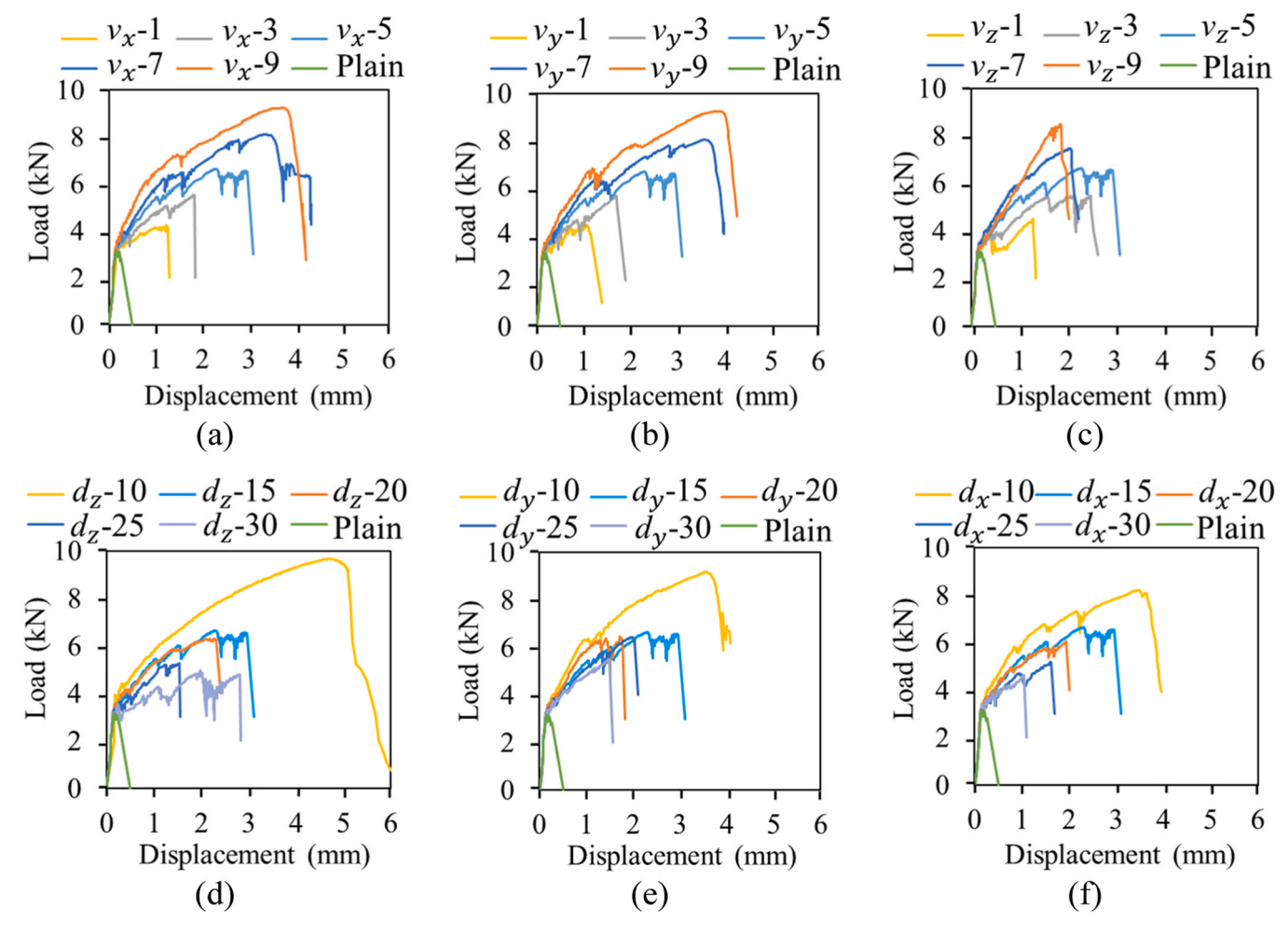


Fig. 12. Load-deflection curves of APCC beams with different design parameters: (a)  $v_x$ , (b)  $v_y$ , (c)  $v_z$ , (d)  $d_x$ , (e)  $d_y$ , and (f)  $d_z$ .

Cracks initiate from the bottom of the sections with transverse polymer filaments and propagate toward the top of the beam. The cracking process and crack patterns are consistent with the experimental testing results (Section 3). With the increase of the applied load, more cracks are generated, and the crack severity is increased. Besides the vertical cracks, horizontal cracks are also generated. Finally, the beam fails with major cracks in concrete and rupture of polymer filaments at the cracked sections.

When concrete is cracked, the interaction between polymer and concrete helps arrests cracks and hinders the propagation of the cracks because of the high ductility of polymer and debonding between polymer and concrete. The debonding between ABS filaments and concrete is indicated by the horizontal cracks in the beams. The debonding helps distribute the localized deformation caused by cracks over a longer length and thus reduce the peak strain [55]. The redistribution of the crack-induced deformation thus alleviates the stress concentration at crack tips and hinders the propagation of cracks toward the top surface of the beams, as shown in Fig. 15. The above damage process is different from that of plain concrete, which is brittle and fractures suddenly after a crack is generated at the bottom of the beam, because the crack propagates toward the top surface of the beam rapidly due to the stress concentration at the crack tip. Such a delay of the development of cracks benefits the APCC beams by increasing their flexural strengths.

The presence of polymer filaments and the occurrence of interfacial debonding between polymer filaments and concrete enhance the energy dissipation capability of APCC beams. The effect of design variables on the energy dissipation of APCC beams is shown in Fig. 16. Increasing  $v_x$  and  $v_y$  increases the energy dissipation; decreasing  $d_x$ ,  $d_y$  and  $d_z$ 

increases the energy dissipation; and increase  $v_z$  first increases and then decreases the energy dissipation.

#### 3.3. Variable importance

The effect of the design variables on  $\delta$  and  $\beta$  is shown in Fig. 17. The data values of the interquartile ranges of the box and whisker plot of  $\delta$  and  $\beta$  are listed in **Table A2** in the Appendix. The lower and upper limits of a box show the first quartile  $(Q_1)$  and third quartile  $(Q_3)$ . The minimum and maximum values of  $\delta$  and  $\beta$  for each variable are represented by the vertical lines of each box. The mean values of  $\delta$  and  $\beta$  for each design variable are shown by symbol "×". The interquartile range (IQR) is the center of a dataset and shown by the box height. The IQR is the difference between the lower quartile  $(Q_1)$  and the upper quartile  $(Q_3)$ .

In Fig. 17,  $v_x$  and  $v_y$  exhibited comparable effects on  $\delta$  and  $\beta$ , as evidenced by their comparable lengths of the box and whisker plot. Along the Z direction, the effect of adjacent filament spacing is larger than the effect of filament dimensions on the flexural properties. Decreasing the spacing between adjacent filaments along Z direction increases  $\delta$  and  $\beta$ . The results show that  $d_z$  has the highest effect on the results of  $\delta$  and  $\beta$ , with lengths of 2.49 and 13.70, respectively, as evidenced by the higher interquartile range compared with the other design variables.

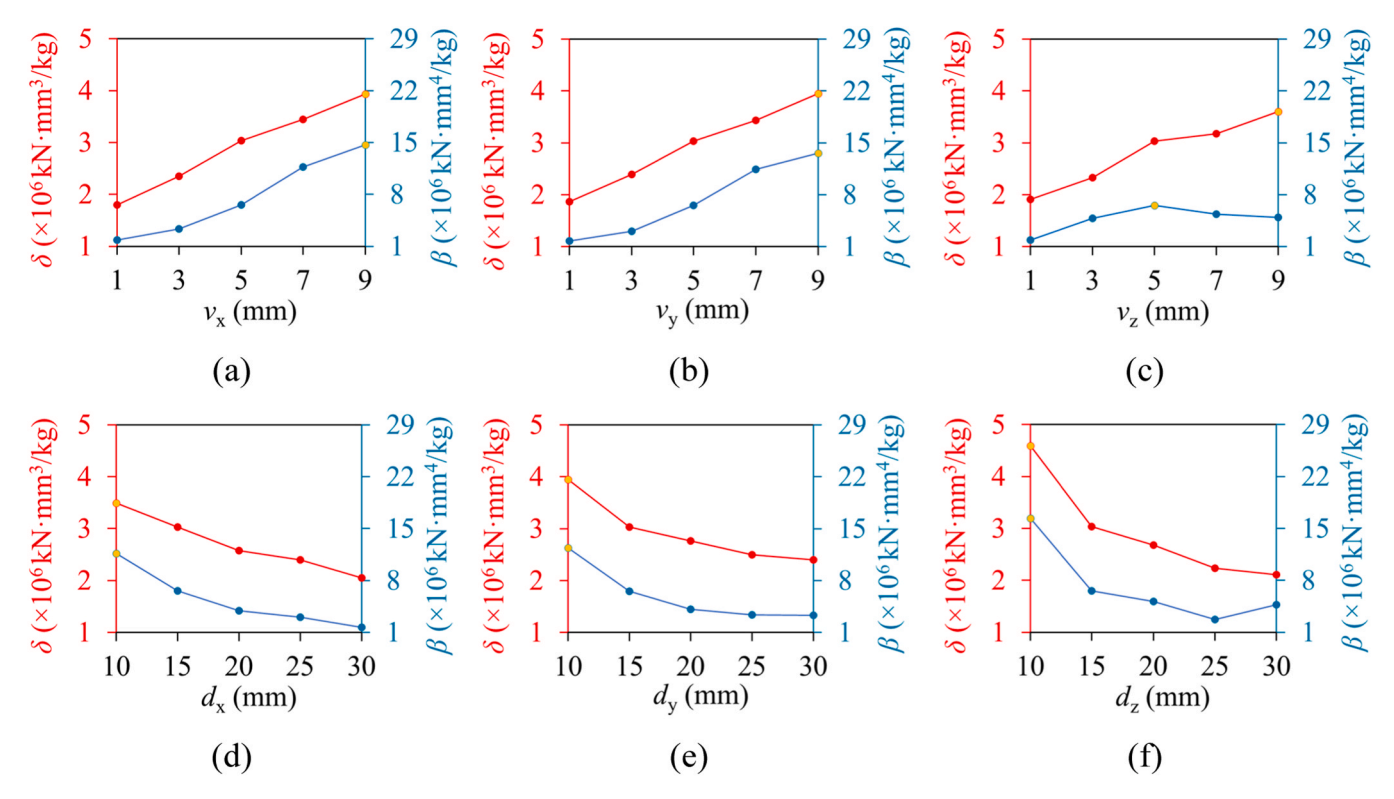


Fig. 13. Results of the specific strength ( $\delta$ ) and specific toughness ( $\beta$ ) of APCC with different design parameters: (a)  $\nu_x$ , (b)  $\nu_y$ , (c)  $\nu_z$ , (d)  $d_x$ , (e)  $d_y$ , and (f)  $d_z$ .

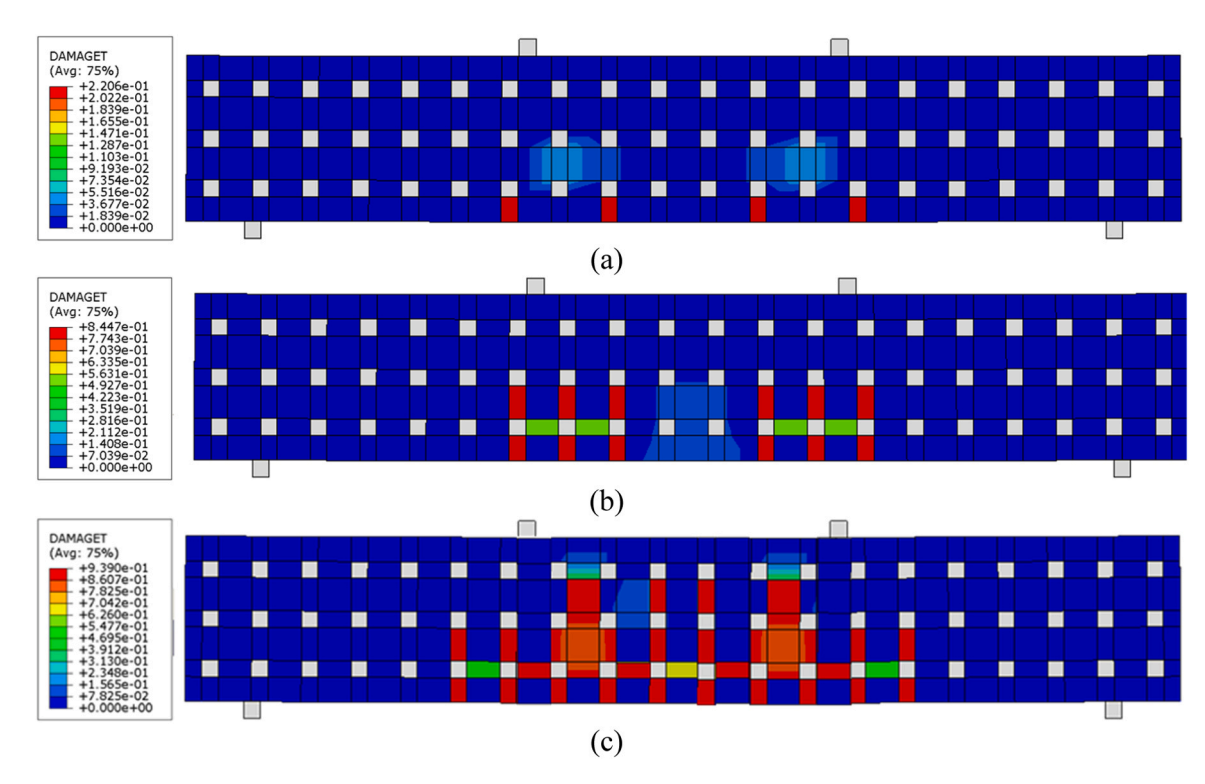


Fig. 14. Simulation results of the development of cracks in the initial design of an APCC beam under different mid-span deflections: (a) 0.6 mm, (b) 1.9 mm, and (c) 5.0 mm.

# 4. Design optimization

### 4.1. Prediction results

The sequential surrogate model, specifically a Kriging model, was

used to predict the specific flexural strength of APCC. To train the predictive model, initial datasets were generated using the finite element model for training and test. More samples were sequentially added to the training dataset to improve the accuracy of the model. In this study, an initial dataset was established using the results from 60 finite element

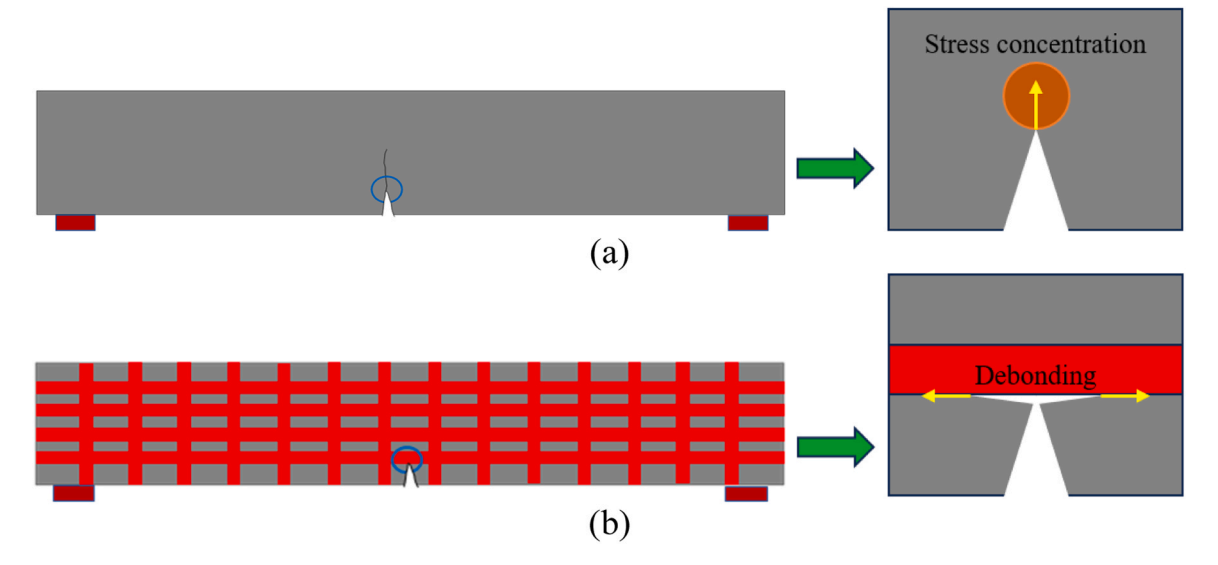


Fig. 15. Propagation and arrestment of cracks in (a) plain concrete, and (b) APCC beam.

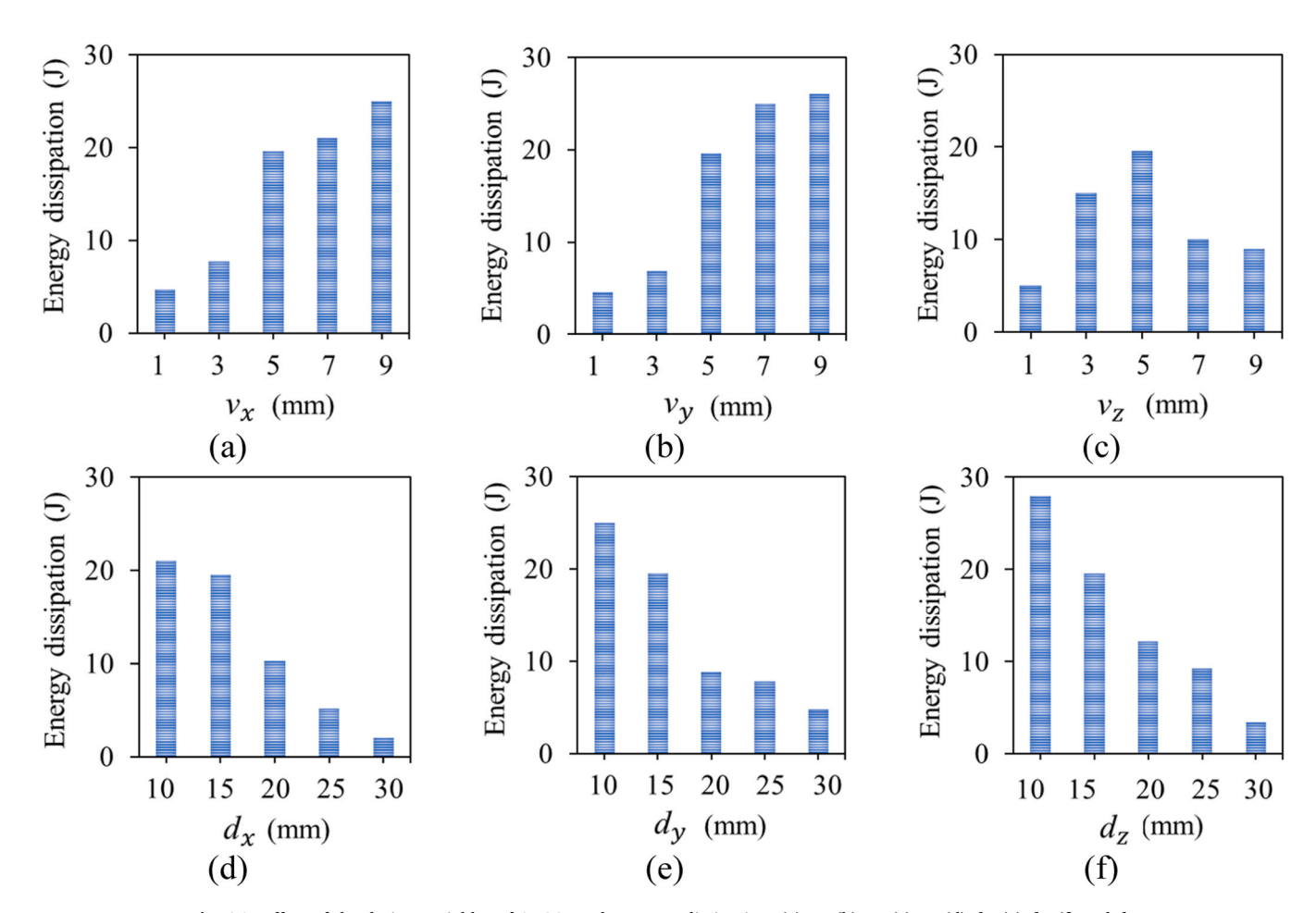
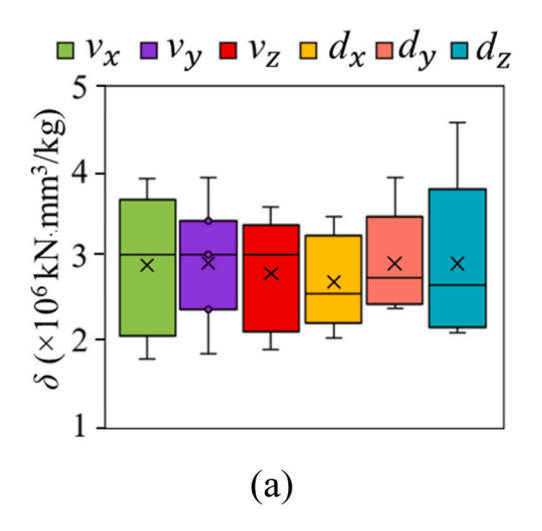


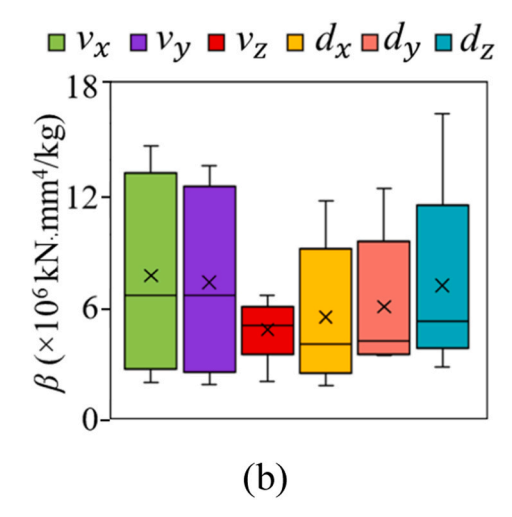
Fig. 16. Effect of the design variables of APCC on the energy dissipation: (a)  $v_x$ , (b)  $v_y$ , (c)  $v_z$ , (d)  $d_x$ , (e)  $d_y$ , (f) and  $d_z$ .

models. Another 50 finite element models were established to generate new samples to enlarge the training dataset. The performance of this surrogate model was then evaluated by comparing its predictions with XGBoost model [56], with hyperparameters optimized via Azure AutoML [57]. The predicted results are compared with the actual results, as shown in Fig. 18. The actual results were obtained from the finite element model, and the prediction results were obtained from the

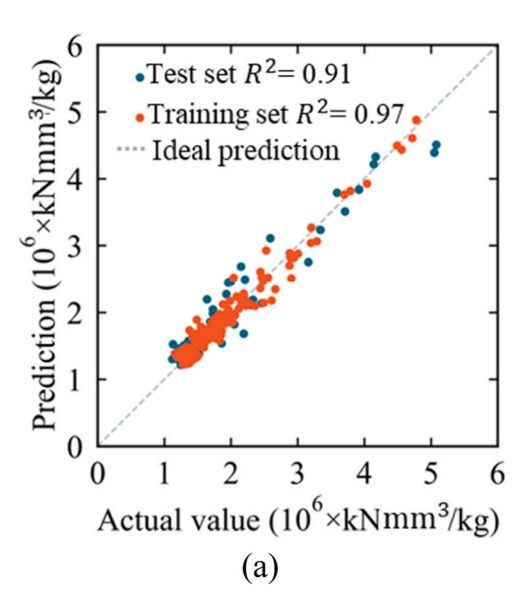
sequential surrogate model and automated machine learning, specifically XGBoost model.

The performance metrics of the training and test datasets are shown in Table 8. The  $R^2$  value of training set using the sequential surrogate model increases from 0.87 to 0.97, and the  $R^2$  value of test set using the sequential surrogate model increases from 0.80 to 0.91. Such an improvement reveals the high performance of the sequential surrogate





**Fig. 17.** Box and whisker plots: (a) specific strength ( $\delta$ ), and (b) specific toughness ( $\beta$ ).



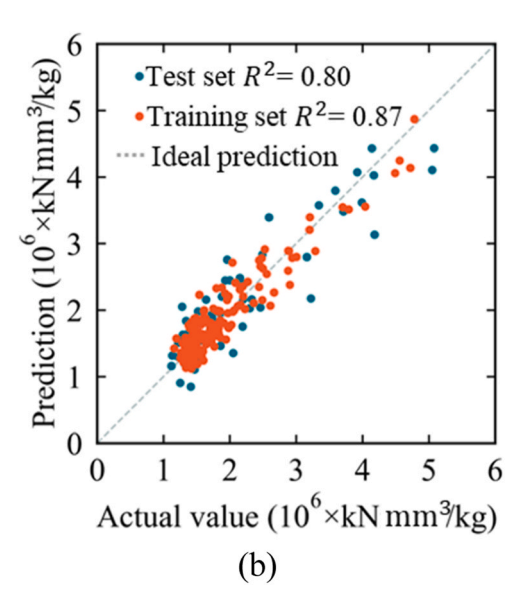


Fig. 18. Comparison of the prediction and actual results of the specific flexural strength: (a) sequential surrogate model, and (b) automated machine learning model.

 Table 8

 Performance metrics of the machine learning models.

Dataset	Performance	Specific flexural strength (×10 <sup>6</sup> kN·mm <sup>3</sup> /kg)				
	metrics	Automated machine learning	Sequential surrogate model			
Training	$R^2$	0.87	0.97			
	RMSE	0.16	0.06			
Test	$R^2$	0.80	0.91			
	RMSE	0.20	0.12			

model which enhances the performance of a prediction model based on the same dataset. The  $\mathbb{R}^2$  value of the test dataset is higher than 0.91, shows that the sequential surrogate model has a satisfactory accuracy

and generalizability, ensuring that the predictive model can be utilized to design APCC.

#### 4.2. Optimization results

The results of the optimal design and initial design of APCC are listed in Table 9. The specific flexural strength and specific toughness of the optimal design are increased by 197% and 234%, respectively, compared with the initial design. The spacings between adjacent filaments were not narrower than 3 mm, ensuring that cement mortar can flow and fill the gaps of polymer lattices, aiming at effective bonding and integrity of the composite material.

The flexural properties of the optimal design, the initial design, and plain concrete beams are compared in Fig. 19. The finite element

**Table 9**Comparison between initial and optimal design.

Designation	Designation Dimension (mm)						δ	β	Improvement (%)	
	$\nu_x$	$\nu_y$	$\nu_z$	$d_x$	$d_{y}$	$d_z$	$(\times 10^6 \text{ kN} \cdot \text{mm}^3/\text{kg})$	$(\times 10^6 \text{ kN} \cdot \text{mm}^4/\text{kg})$	δ	β
Initial	5	5	5	15	15	15	3.03	6.59	197 %	234 %
Optimal	9	9	9	15	15	15	9.04	22.0		

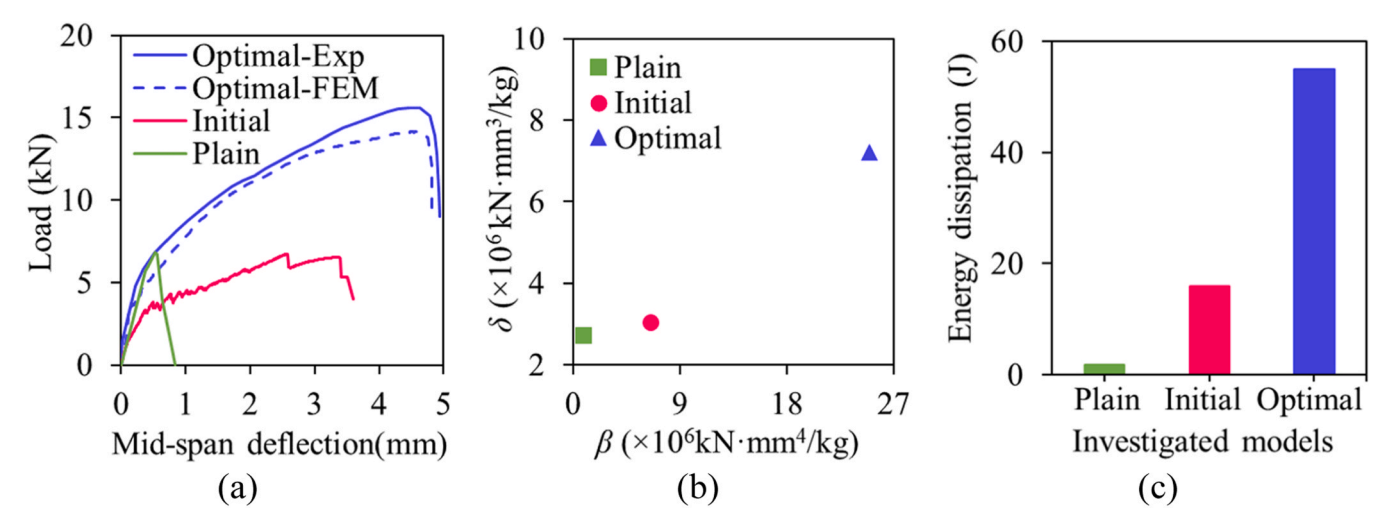


Fig. 19. Finite element analysis results of APCC beams made using the optimal design, initial design, and plain concrete: (a) load-deflection curve, (b) specific flexural strength and specific toughness, and (c) energy dissipation.

analysis results agree with the experimental results. Compared with plain concrete, the optimal design increases the specific flexural strength, specific toughness, and energy dissipation by 230 %, 2245 %, and 2841 %, respectively.

The energy dissipation histories of concrete and polymer lattices in the loading process are shown in Fig. 20. Before concrete is cracked, concrete matrix absorbs more energy than polymer lattices since the volume of concrete is larger than that of polymer lattices. After concrete is cracked, polymer lattices absorb more energy due to their higher tensile strength and ductility.

The results of the specific flexural strength ( $\delta$ ) and toughness ( $\beta$ ) of the APCC designed in this work are compared with the results from previous research, as shown in Fig. 21. The data are listed in **Table A3** in the Appendix. The APCC designed at 7 days achieved the highest  $\delta$  and  $\beta$  in comparison with normal concrete (NC), FRC, UHPC, ECC, and previous APCC tested at 28 days. This indicates that the optimal design of APCC achieves its critical performance metrics within the first 7 days, surpassing even the longer-term strength and toughness values. The high flexural properties and light weight make APCC an interesting material for structural applications, especially under dynamic loading conditions, such as earthquake and impact loading conditions. The anticipated structural members include, but are not limited to, walls, floor slabs, and stairs of buildings, barriers of highways and bridges, and decks of

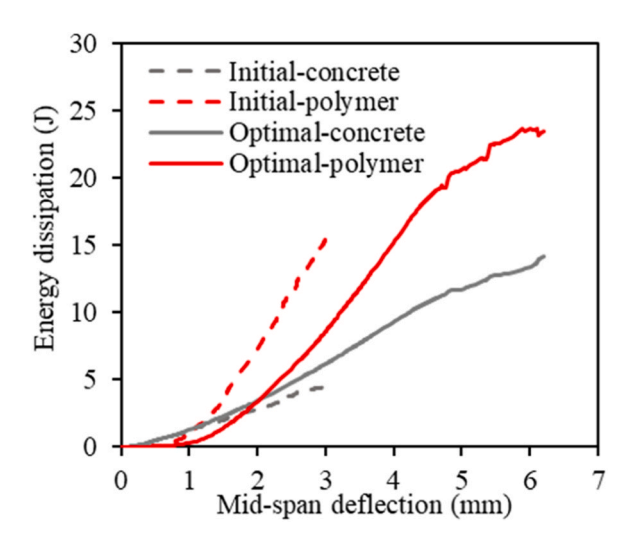
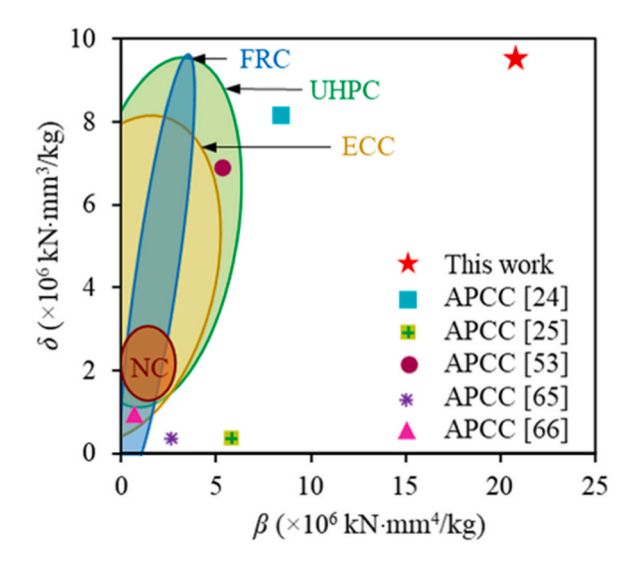


Fig. 20. Energy dissipation in concrete and polymer sections of initial and optimal design.



**Fig. 21.** Comparison of the specific strength ( $\delta$ ) and specific toughness ( $\beta$ ) of various materials.

footbridges. Further research is necessary to evaluate the performance of structural members constructed using APCC materials.

#### 5. Conclusions

This paper presents an AI framework for efficient design of APCC, aimed to achieve high flexural strength, high toughness, and low density. The following conclusions are drawn:

- The proposed AI framework is effective in designing APCC with high specific flexural strength and high specific toughness, while also ensuring castability of concrete. Compared with the beam made of plain concrete, the proposed design of APCC beam increased the specific flexural strength, specific toughness, and energy dissipation by 230 %, 2245 %, and 2841 %, respectively. The APCC beams achieved the strain-hardening property and exhibited multiple cracks which increased the deformability and toughness.
- The underlying mechanisms of enhancing the flexural properties by polymer lattices were revealed. The flexural strength is increased through the bridging effect of polymer lattices that hinder the widening of cracks due to the high tensile strength of the polymer.

The toughness is increased by the increase of the flexural strength and ductility of APCC via multiple mechanisms. First, the presence of polymer lattices reduces the area of concrete periodically, promoting the generation of multiple cracks. Second, the polymer lattices hinder the fracture failure of APCC by bridging the cracks. Third, the presence of polymer lattices promotes the occurrence of horizontal cracks along the interface between polymer and concrete. An interesting finding is that the polymer lattices do not hinder the initiation of cracks. Instead, the polymer lattices promote the initiation of cracks and can control the propagation of cracks. The polymer lattices hindered catastrophic propagation of vertical cracks and promoted the initiation and development of horizontal cracks. In summary, the use of polymer lattices imparts various mechanisms to hinder failure and dissipate energy.

• The parametric study uncovered the effect of the design variables of polymer lattices on the specific flexural strength and toughness of APCC. The key findings include: (i) Increasing polymer filament dimensions and decreasing the spacing between adjacent filaments in both X and Y directions enhanced the specific flexural strength and toughness. (ii) Increasing polymer filament dimensions from 1 mm to 9 mm increased the specific flexural strength and toughness by 112 % and 679 %, respectively. Decreasing the distance between polymer filaments from 30 mm to 10 mm increased the specific flexural strength and toughness by 65 % and 275 %, respectively. (iii) Increasing the dimensions of polymer filament along the Z direction first increased the specific flexural strength and toughness due to the arrestment of cracks and then decreased the specific flexural strength and toughness due to the reduction of the effective area of concrete.

This research is limited to the design, fabrication, and testing of small-scale beams with ABS lattices embedded in concrete mortar. Further research is necessary to establish a holistic understanding of the performance of the proposed approach in large-scale applications. It is envisioned that the approach can be applied to the design of APCC for

large-scale structures because 3D printed polymer lattices can be assembled to generate large-scale polymer lattices for casting various structural components. It is also interesting to test the performance of other types of polymers such as polylactic acid and cement-based materials such as ultra-high-performance concrete and strain-hardening cementitious composites.

# CRediT authorship contribution statement

Rojyar Barhemat: Writing – review & editing, Writing – original draft, Visualization, Validation, Supervision, Software, Methodology, Investigation, Formal analysis, Data curation, Conceptualization. Soroush Mahjoubi: Writing – review & editing, Writing – original draft, Visualization, Validation, Software, Methodology, Investigation, Formal analysis, Data curation. Weina Meng: Writing – review & editing, Supervision, Resources, Project administration, Investigation, Funding acquisition, Validation, Supervision, Software, Resources, Project administration, Wethodology, Investigation, Funding acquisition, Formal analysis, Data curation, Conceptualization.

#### **Declaration of Competing Interest**

The authors declare the following financial interests/personal relationships which may be considered as potential competing interests: Weina Meng received funding from US National Science Foundation.

#### Data availability

Data will be made available on request.

#### Acknowledgement

This research was funded by the National Science Foundation of the United States [award number: CMMI-2046407].

# **Appendix**

**Table A1** shows the results of the mechanical properties of the investigated APCC beams.

**Table A1**Mechanical properties of the investigated APCC beams

Design variables	Designation	Density (kg/m³)	Strength (kN)	Toughness (kN.mm)	$\delta$ (×10 <sup>6</sup> kN·mm <sup>3</sup> /kg)	$\beta$ (×10 <sup>6</sup> kN·mm <sup>4</sup> /kg)
$v_x$	$\nu_x$ -1	2310	4.21	4.41	1.79	1.88
	$v_x$ -3	2226	5.53	7.81	2.35	3.32
	$v_x$ -5	2142	6.64	16.4	3.03	7.66
	$v_x$ -7	2058	8.10	27.55	3.45	11.72
	$v_x$ -9	1973	9.25	34.50	3.93	14.70
$v_{\rm y}$	$\nu_{\rm y}{-}1$	2299	4.36	4.08	1.86	1.74
	$v_y$ -3	2220	5.59	7.25	2.39	3.10
	$v_y$ -5	2142	6.64	16.4	3.03	7.66
	$v_{y}$ -7	2063	8.02	26.66	3.43	11.40
	$v_y$ -9	1985	9.23	31.80	3.95	13.60
$v_z$	$v_z$ -1	2312	4.49	4.46	1.91	1.90
	$v_z$ -3	2227	5.49	11.31	2.33	4.81
	$v_z$ -5	2142	6.64	16.4	3.03	7.66
	$v_z$ -7	2057	7.47	12.65	3.17	5.37
	$v_z$ -9	1972	8.48	11.67	3.60	4.96
$d_x$	$d_x$ -10	2057	8.21	27.44	3.49	11.74
	$d_x$ -15	2142	6.64	16.4	3.03	7.66
	$d_x$ -20	2184	6.05	9.23	2.58	3.93
	$d_{x}$ -25	2226	5.17	6.58	2.40	3.05
	$d_x - 30$	2226	4.64	3.76	2.05	1.66
$d_{y}$	$d_y$ -10	2076	9.2	28.87	3.95	12.43
	$d_y$ -15	2142	6.64	16.4	3.03	7.66
	$d_{\rm y}$ -20	2207	6.46	9.18	2.76	4.10

(continued on next page)

Table A1 (continued)

Design variables	Designation	Density (kg/m³)	Strength (kN)	Toughness (kN.mm)	$\delta$ (×10 <sup>6</sup> kN·mm <sup>3</sup> /kg)	$\beta$ (×10 <sup>6</sup> kN·mm <sup>4</sup> /kg)
	$d_{_{Y}}$ -25	2207	6.44	10.20	2.52	3.40
	$d_{\gamma}$ -30	2207	5.52	6.54	2.44	3.30
$d_z$	$d_z$ -10	2046	10.82	38.58	4.60	16.41
	$d_z - 15$	2142	6.64	16.4	3.03	7.66
	$d_z$ -20	2195	6.31	12.16	2.68	5.16
	$d_z$ -25	2227	5.27	6.37	2.24	2.70
	$d_z - 30$	2248	4.97	11.06	2.11	4.70

**Table A2** shows the results of the interquartile ranges of the box and whisker plot.

**Table A2**Interquartile range of the box and whisker plot

Designation	$\delta$ (×10 <sup>6</sup> kN·r	nm³/kg)			β (×10 <sup>6</sup> kN·n	nm <sup>4</sup> /kg)		
	$\overline{Q_1}$	$Q_2$	$Q_3$	Range	$\overline{Q_1}$	$Q_2$	$Q_3$	Range
$\nu_x$	1.79	2.91	3.93	2.14	1.88	7.63	14.70	12.82
$\nu_{\gamma}$	1.87	2.93	3.95	2.08	1.74	7.29	13.60	11.86
$v_z$	1.91	2.81	3.60	1.69	1.89	4.73	6.59	4.70
$d_x$	2.05	2.71	3.49	1.44	1.66	5.38	11.70	10.04
$d_{y}$	2.40	2.93	3.95	1.55	3.30	5.96	12.40	9.10
$d_z$	2.11	2.93	4.60	2.49	2.70	7.11	16.40	13.70

**Table A3** shows comparison between the specific strength ( $\delta$ ) and specific toughness ( $\beta$ ) of this work and previous research.

**Table A3**Comparison between proposed framework and previous research

Category	Reference  [51]	$\frac{\delta}{(\times 10^6 \text{ kN•mm}^3/\text{kg})}$ $\frac{2.72}{}$	$\frac{\beta}{(\times 10^6 \text{ kN•mm}^4/\text{kg})}$ $0.87$	Difference with this work (%)	
				δ	β
				-68 %	-96 %
FRC	[4]	0.3	0.45	−97 %	-98 %
		0.13	0.26	-98 %	<b>-99</b> %
		0.10	0.21	<b>-99</b> %	<b>-99</b> %
		0.09	0.16	<b>-99</b> %	<b>-99</b> %
		0.08	0.13	<b>-99</b> %	<b>-99</b> %
	[58]	6.05	7.52	-28~%	<b>-63</b> %
	[59]	8.3	2.9	-2%	-85 %
	[60]	9.54	3.30	-12~%	-83 %
	[61]	0.23	5.67	<b>−97</b> %	<b>-99</b> %
		0.26	7.94	97 %	-100~%
	[62]	4.35	1.74	48 %	-91 %
	[63]	4.00	1.98	-53 %	<b>-90</b> %
ECC	[64]	8.32	8.32	-2.0~%	-59 %
	[65]	1.38	0.35	-84 %	-98 %
		9.53	3.81	12 %	-81 %
	[66]	2.06	3.09	<b>−75</b> %	-84 %
		2.06	2.06	<b>−75</b> %	-90 %
		2.00	3.30	<b>-767</b> %	-84 %
		2.54	4.70	<b>−70</b> %	<b>-77</b> %
		1.87	3.28	-78 %	-84 %
		1.71	2.13	-80 %	-90 %
		0.83	1.25	−90 %	-94 %
		1.87	3.25	− <b>78</b> %	-84 %
UHPC	[67]	2.15	0.76	− <b>75</b> %	-99 %
	[0/]	2.87	1.00	−66 %	−95 %
		6.63	3.65	-22 %	-82 %
		3.94	2.17	-54 %	−89 %
	[68]	3.23	2.42	−62 %	-88 %
	[69]	6.10	4.57	-28 %	−77 %
	[70]	7.89	1.97	-7 %	-90 %
	[24]	4.66	0.23	-45 %	-98 %
APCC	[25]	0.03	6.08	-100 %	− <b>70</b> %
	[71]	6.87	5.15	-19 %	−75 % −75 %
	[24]	8.38	7.93	-1 %	-61 %
	[72]	0.36	1.62	-1 % -96 %	-92 %
	[73]	1.92	0.27	-77 %	-92 % -98 %
This work	[/3]	9.04	22.0	-// 70	- 30 70

#### References

- [1] I.N. York, I. Europe, Concrete needs to lose its colossal carbon footprint, Nature (2021) 593–594, https://doi.org/10.1038/d41586-021-02612-5.
- [2] Q. Moya, O. Pons, Improving the design and production data flow of a complex curvilinear geometric Glass Reinforced Concrete façade, Autom. Constr. 38 (2014) 46–58, https://doi.org/10.1016/j.autcon.2013.10.025.
- [3] F. Kang, J. Liu, J. Li, S. Li, Concrete dam deformation prediction model for health monitoring based on extreme learning machine, Struct. Control Health Monit. 24 (10) (2017) e1997, https://doi.org/10.1002/stc.1997.
- [4] D. Chen, G. Sun, M. Meng, X. Jin, Q. Li, Flexural performance and cost efficiency of carbon/basalt/glass hybrid FRP composite laminates, Thin Walled Struct. 142 (2019) 516–531, https://doi.org/10.1016/j.tws.2019.03.056.
- [5] L. Fan, W. Meng, L. Teng, K.H. Khayat, Effect of steel fibers with galvanized coatings on corrosion of steel bars embedded in UHPC, Compos. Part B: Eng. 177 (2019) 107445, https://doi.org/10.1016/j.compositesb.2019.107445.
- [6] L. Fan, Y. Bao, W. Meng, G. Chen, In-situ monitoring of corrosion-induced expansion and mass loss of steel bar in steel fiber reinforced concrete using a distributed fiber optic sensor, Compos. Part B: Eng. 165 (2019) 679–689, https:// doi.org/10.1016/i.compositesb.2019.02.051.
- [7] H.H. Nguyễn, P.H. Nguyễn, Q.H. Lương, W. Meng, B.Y. Lee, Mechanical and autogenous healing properties of high-strength and ultra-ductility engineered geopolymer composites reinforced by PE-PVA hybrid fibers, Cem. Concr. Compos. 142 (2023) 105155, https://doi.org/10.1016/j.cem.concomp.2023.105155.
- 142 (2023) 105155, https://doi.org/10.1016/j.cemconcomp.2023.105155.
   Y. Zeng, X. Zhou, A. Tang, P. Sun, Mechanical properties of chopped basalt fiber-reinforced lightweight aggregate concrete and chopped polyacrylonitrile fiber reinforced lightweight aggregate concrete, Materials 13 (7) (2020) 1715, https://doi.org/10.3390/ma13071715.
- [9] J. Du, W. Meng, K.H. Khayat, Y. Bao, P. Guo, Z. Lyu, A. Abu-obeidah, H. Nassif, H. Wang, New development of ultra-high-performance concrete (UHPC), Compos. Part B: Eng. 224 (2021) 109220, https://doi.org/10.1016/j. compositesb 2021 109220
- [10] P. Guo, W. Meng, Y. Bao, Automatic identification and quantification of dense microcracks in high-performance fiber-reinforced cementitious composites through deep learning-based computer vision, Cem. Concr. Res. 148 (2021) 106532, https://doi.org/10.1016/j.cemconres.2021.106532.
- [11] M. Xu, Y. Bao, K. Wu, T. Xia, H. Clack, H. Shi, V.C. Li, Influence of TiO2 incorporation methods on NOx abatement in Engineered Cementitious Composites, Constr. Build. Mater. 221 (2019) 375–383, https://doi.org/10.1016/j.conbuildmat.2019.06.053.
- [12] W. Meng, K.H. Khayat, Mechanical properties of ultra-high-performance concrete enhanced with graphite nanoplatelets and carbon nanofibers, Compos. Part B: Eng. 107 (2016) 113–122, https://doi.org/10.1016/j.compositesb.2016.09.069.
- [13] W. Meng, M. Valipour, K.H. Khayat, Optimization and performance of cost-effective ultra-high performance concrete, Mater. Struct. 50 (2017) 1–16, https://link.springer.com/article/10.1617/s11527-016-0896-3.
- [14] W. Meng, K.H. Khayat, Improving flexural performance of ultra-high-performance concrete by rheology control of suspending mortar, Compos. Part B: Eng. 117 (2017) 26–34, https://doi.org/10.1016/j.compositesb.2017.02.019.
- [15] L. Teng, W. Meng, K.H. Khayat, Rheology control of ultra-high-performance concrete made with different fiber contents, Cem. Concr. Res. 138 (2020) 106222, https://doi.org/10.1016/j.cemconres.2020.106222.
- [16] S. Iqbal, A. Ali, K. Holschemacher, T.A. Bier, Mechanical properties of steel fiber reinforced high strength lightweight self-compacting concrete (SHLSCC), Constr. Build. Mater. 98 (2015) 325–333, https://doi.org/10.1016/j. conbuildmat.2015.08.112.
- [17] Y. Liu, Z. Zhang, C. Shi, D. Zhu, N. Li, Y. Deng, Development of ultra-high performance geopolymer concrete (UHPGC): Influence of steel fiber on mechanical properties, Cem. Concr. Compos. 112 (2020) 103670, https://doi.org/10.1016/j. cemconcomp.2020.103670.
- [18] A. Mudadu, G. Tiberti, F. Germano, G.A. Plizzari, A. Morbi, The effect of fiber orientation on the post-cracking behavior of steel fiber reinforced concrete under bending and uniaxial tensile tests, Cem. Concr. Compos. 93 (2018) 274–288, https://doi.org/10.1016/j.cemconcomp.2018.07.012.
- [19] Y. Xue, W. Wang, F. Han, Enhanced compressive mechanical properties of aluminum based auxetic lattice structures filled with polymers, Compos. Part B: Eng. 171 (2019) 183–191, https://doi.org/10.1016/j.compositesb.2019.05.002.
- [20] W. Xu, S. Jambhulkar, Y. Zhu, D. Ravichandran, M. Kakarla, B. Vernon, D.G. Lott, J.L. Cornella, O. Shefi, G. Miquelard-Garnier, Y. Yang, 3D printing for polymer/ particle-based processing: a review, Compos. Part B: Eng. 223 (2021) 109102, https://doi.org/10.1016/j.compositesb.2021.109102.
- [21] X.G. Zhang, X. Ren, W. Jiang, X.Y. Zhang, C. Luo, Y. Zhang, Y.M. Xie, A novel auxetic chiral lattice composite: experimental and numerical study, Compos. Struct. 282 (2022) 115043, https://doi.org/10.1016/j.compstruct.2021.115043.
- [22] H.C. Luo, X. Ren, Y. Zhang, X.Y. Zhang, X.G. Zhang, C. Luo, X. Cheng, Y.M. Xie, Mechanical properties of foam-filled hexagonal and re-entrant honeycombs under uniaxial compression, Compos. Struct. 280 (2022) 114922, https://doi.org/ 10.1016/j.compstruct.2021.114922.
- [23] X. Guo, J. Ding, X. Li, S. Qu, J.Y.H. Fuh, W.F. Lu, X. Song, W. Zhai, Interpenetrating phase composites with 3D printed triply periodic minimal surface (TPMS) lattice structures, Compos. Part B: Eng. 248 (2023) 110351, https://doi.org/10.1016/j. cemconcomp.2023.105046.
- [24] B. Salazar, P. Aghdasi, I. Williams, C. Ostertag, H. Taylor, Polymer lattice-reinforcement for enhancing ductility of concrete, Mater. Des. 196 (2020) 109184, https://doi.org/10.1016/j.matdes.2020.109184.

- [25] Y. Xu, B. Šavija, Development of strain hardening cementitious composite (SHCC) reinforced with 3D printed polymeric reinforcement: mechanical properties, Compos. Part B: Eng. 174 (2019) 107011, https://doi.org/10.1016/j.compositesb.2019.107011.
- [26] R. Zhong, X. Ren, X.Y. Zhang, C. Luo, Y. Zhang, Y.M. Xie, Mechanical properties of concrete composites with auxetic single and layered honeycomb structures, Constr. Build. Mater. 322 (2022) 126453, https://doi.org/10.1016/j. conbuildmat.2022.126453.
- [27] M. Chen, Z. Chen, Y. Xuan, T. Zhang, M. Zhang, Static and dynamic compressive behaviour of 3D printed auxetic lattice reinforced ultra-high performance concrete, Cem. Concr. Compos. 139 (2023) 105046, https://doi.org/10.1016/j. cemconcomp.2023.105046.
- [28] H. Zhou, K. Jia, X. Wang, M.X. Xiong, Y. Wang, Experimental and numerical investigation of low velocity impact response of foam concrete filled auxetic honeycombs, Thin Walled Struct. 154 (2020) 106898, https://doi.org/10.1016/j. tws.2020.106898.
- [29] Z. Wan, Y. Zhang, Y. Xu, B. Šavija, Self-healing cementitious composites with a hollow vascular network created using 3D-printed sacrificial templates, Eng. Struct. 289 (2023) 116282, https://doi.org/10.1016/j.engstruct.2023.116282.
- [30] M.D. Mckay, R.J. Beckman, W.J. Conover, Comparison of three methods for selecting values of input variables in the analysis of output from a computer code, Technometrics 42 (1) (2000) 55–61, https://www.tandfonline.com/doi/abs/ 10.1080/00401706.2000.10485979.
- [31] S.-S. Jin, H.-J. Jung, Sequential surrogate modeling for efficient finite element model updating, Comput. Struct. 168 (2016) 30–45, https://doi.org/10.1016/j. compstruc 2016 02 005
- [32] A. Kaveh, S. Mahjoubi, Lion pride optimization algorithm: a meta-heuristic method for global optimization problems, Sci. Iran. 25 (2018) 3113–3132, https://doi.org/ 10.24200/SCI.2018.20833.
- [33] ABAQUS/CAE Version 2017. Software for Technical Computation. Simulia Corp: Providence, RI, United States, 2017. https://www.3ds.com/products-services/simulia/products/abaqus/abaquscae/.
- [34] S. Mahjoubi, R. Barhemat, W. Meng, Y. Bao, Al-guided auto-discovery of low-carbon cost-effective ultra-high performance concrete (UHPC), Resour. Conserv. Recycl. 189 (2023) 106741, https://doi.org/10.1016/j.resconrec.2022.106741.
- [35] S. Mahjoubi, R. Barhemat, P. Guo, W. Meng, Y. Bao, Prediction and multi-objective optimization of mechanical, economical, and environmental properties for strainhardening cementitious composites (SHCC) based on automated machine learning and metaheuristic algorithms, J. Clean. Prod. 329 (2021) 129665, https://doi.org/ 10.1016/j.iclepro.2021.129665.
- [36] B.K. Nagesha, V. Dhinakaran, M.V. Shree, K.P.M. Kumar, D. Chalawadi, T. Sathish, Review of characterization and impacts of the lattice structure in additive manufacturing, Mater. Today.: Proc. 21 (2020) 916–919, https://doi.org/10.1016/ i.matur. 2019.08, 158
- [37] R.L. Iman, J.C. Helton, J.E. Campbell, An approach to sensitivity analysis of computer models: Part I—Introduction, input variable selection and preliminary variable assessment, J. Qual. Technol. 13 (3) (2018) 174–183, https://doi.org/ 10.1080/00224065.1981.11928748.
- [38] J.L. Loeppky, J. Sacks, W.J. Welch, Choosing the sample size of a computer experiment: a practical guide, Technometrics 51 (4) (2009) 366–376, https://doi. org/10.1198/TECH.2009.08040.
- [39] Orr, M.J., 1996. Introduction to radial basis function networks. Technical Report, Center for Cognitive Science, University of Edinburgh. https://faculty.cc.gatech.edu/~isbell/tutorials/rbf-intro.pdf.
- [40] J.P. Kleijnen, Kriging metamodeling in simulation: a review, Eur. J. Oper. Res. 192 (3) (2009) 707–716, https://doi.org/10.1016/j.ejor.2007.10.013.
- [41] N. Gupta, Artificial neural network, Netw. Complex Syst. 3 (1) (2013) 24–28, https://doi.org/10.1007/978-1-4615-0377-4\_5.
- [42] J. Eason, S. Cremaschi, Adaptive sequential sampling for surrogate model generation with artificial neural networks, Comput. Chem. Eng. 68 (2014) 220–232, https://doi.org/10.1016/j.compchemeng.2014.05.021.
- [43] D.R. Jones, A taxonomy of global optimization methods based on response surfaces, J. Glob. Optim. 21 (2001) 345–383, https://doi.org/10.1023/A: 1012771025575.
- [44] Forrester, A.I.J., Sobester, A., Keane, A.J., 2008. Engineering design via surrogate modelling: a practical guide. John Wiley & Sons. 10.1002/9780470770801.
- [45] Santner, T.J., Williams, B.J., Notz, W.I., Williams, B.J., 2003. The design and analysis of computer experiments. New York: Springer. https://www.asc.ohiostate.edu/santner.1/TJS-BJW-WIN/master-driver.pdf.
- [46] R. Barhemat, S. Mahjoubi, V.C. Li, Y. Bao, Lego-inspired reconfigurable modular blocks for automated construction of engineering structures, Autom. Constr. 139 (2022) 104323, https://doi.org/10.1016/j.autcon.2022.104323.
- [47] S. Mahjoubi, R. Barhemat, Y. Bao, Optimal placement of triaxial accelerometers using hypotrochoid spiral optimization algorithm for automated monitoring of high-rise buildings, Autom. Constr. 118 (2020) 103273, https://doi.org/10.1016/j. autom. 2020.103273
- [48] K.S. Boparai, R. Singh, H. Singh, Development of rapid tooling using fused deposition modeling: a review, Rapid Prototyp. J. 22 (2) (2016) 281–299, https://doi.org/10.1108/RPJ-04-2014-0048.
- [49] ASTM C109 / C109M 20b., 2020. Standard Test Method for Compressive Strength of Hydraulic Cement Mortars (using 2-in. or [50-mm] Cube Specimens). ASTM International, United States. https://www.astm.org/c0109\_c0109m-20.html.
- [50] ACI, 2019. Building code requirements for structural concrete (ACI 318-19) and commentary. https://www.concrete.org/news/newsdetail.aspx?f=51719135.

- [51] Y. Sümer, M. Aktaş, Defining parameters for concrete damage plasticity model, Chall. J. Struct. Mech. 1 (3) (2015) 149–155, https://doi.org/10.20528/ cismec 2015 07 023
- [52] M. Hafezolghorani, F. Hejazi, R. Vaghei, M.S.B. Jaafar, K. Karimzade, Simplified damage plasticity model for concrete, Struct. Eng. Int. 27 (1) (2017) 68–78, https://doi.org/10.2749/101686616X1081.
- [53] S. Neve, J. Du, R. Barhemat, W. Meng, Y. Bao, D. Sarkar, Valorization of vetiver root biochar in eco-friendly reinforced concrete: mechanical, economic, and environmental performance, Materials 16 (6) (2023) 2522, https://doi.org/ 10.3390/ma16062522.
- [54] A. Fadeel, A. Mian, M. Al Rifaie, R. Srinivasan, Effect of vertical strut arrangements on compression characteristics of 3D printed polymer lattice structures: experimental and computational study, J. Mater. Eng. Perform. 28 (2019) 709–716, https://doi.org/10.1007/s11665-018-3810-z.
- [55] X. Tan, S. Mahjoubi, X. Zou, W. Meng, Y. Bao, Metaheuristic inverse analysis on interfacial mechanics of distributed fiber optic sensors undergoing interfacial debonding, Mech. Syst. Signal Process. 200 (2023) 110532, https://doi.org/ 10.1016/j.ymssp.2023.110532.
- [56] T. Chen, C. Guestrin, Xgboost: e scalable tree boosting system, Proc. 22nd acm sigkdd Int. Conf. Knowl. Discov. data Min. (2016) 785–794, https://doi.org/ 10.1145/2939672.2939785.
- [57] M. Copeland, J. Soh, A. Puca, M. Manning, D. Gollob, Microsoft Azure and cloud computing, Microsoft Azur. (2015) 3–26, https://doi.org/10.1007/978-1-4842-1003-7-1
- [58] H. Zhang, P.K. Sarker, Q. Wang, B. He, J.C. Kuri, Z. Jiang, Comparison of compressive, flexural, and temperature-induced ductility behaviours of steel-PVA hybrid fibre reinforced OPC and geopolymer concretes after high temperatures exposure, Constr. Build. Mater. 399 (2023) 132560, https://doi.org/10.1016/j. conbuildmat.2023.132560.
- [59] W. Xu, L. Yang, D. Gao, J. Tang, G. Sun, Y. Zhang, Mechanical properties of seawater-mixed steel fiber reinforced concrete, J. Build. Eng. 73 (2023) 106823, https://doi.org/10.1016/j.jobe.2023.106823.
- [60] S. Zhang, D. Gao, H. Zhu, L. Chen, Z. He, L. Yang, Flexural behavior of seawater-mixed steel fiber reinforced concrete exposed to simulated marine environments, Constr. Build. Mater. 373 (2023) 130858, https://doi.org/10.1016/j.conbuildmat.2023.130858.
- [61] X. Shi, B. Ning, J. Wang, T. Cui, M. Zhong, Improving flexural toughness of foamed concrete by mixing polyvinyl alcohol-polypropylene fibers: an experimental study, Constr. Build. Mater. 400 (2023) 132689, https://doi.org/10.1016/j. conbuildmat.2023.132689.

- [62] R. Babaie, M. Abolfazli, A. Fahimifar, Mechanical properties of steel and polymer fiber reinforced concrete, J. Mech. Behav. Mater. 28 (1) (2019) 119–134, https://doi.org/10.1515/jmbm-2019-0014.
- [63] Y. Wei, Y. Qin, J. Chai, C. Xu, Y. Zhang, X. Zhang, Experimental study on compressive and flexural performances of polypropylene fiber-reinforced concrete, Geofluids (2022), https://doi.org/10.1155/2022/4168918.
- [64] Y. Guan, H. Yuan, Z. Ge, Y. Huang, S. Li, R. Sun, Flexural properties of ECC-concrete composite beam, Adv. Civ. Eng. (2018) 3138759, https://doi.org/10.1155/2018/3138759.
- [65] J. Pan, F. Yuan, M. Luo, K. Leung, Effect of composition on flexural behavior of engineered cementitious composites, Sci. China Technol. Sci. 55 (2012) 3425–3433, https://doi.org/10.1007/s11431-012-4990-7.
- [66] M. Zhu, B. Chen, M. Wu, J. Han, Effects of different mixing ratio parameters on mechanical properties of cost-effective green engineered cementitious composites (ECC), Constr. Build. Mater. 328 (2022) 127093, https://doi.org/10.1016/j. conbuildmat.2022.127093.
- [67] K. Ragalwar, W.F. Heard, B.A. Williams, D. Kumar, R. Ranade, On enhancing the mechanical behavior of ultra-high performance concrete through multi-scale fiber reinforcement, Cem. Concr. Compos. 105 (2020) 103422, https://doi.org/ 10.1016/j.cemconcomp.2019.103422.
- [68] K.R. Akça, M. Ipek, Effect of different fiber combinations and optimisation of an ultra-high performance concrete (UHPC) mix applicable in structural elements, Constr. Build. Mater. 315 (2022) 125777, https://doi.org/10.1016/j. conbuildmat.2021.125777.
- [69] I.Y. Hakeem, F. Althoey, A. Hosen, Mechanical and durability performance of ultrahigh-performance concrete incorporating SCMs, Constr. Build. Mater. 359 (2022) 129430, https://doi.org/10.1016/j.conbuildmat.2022.129430.
- [70] M. Madhkhan, P. Saeidian, Mechanical properties of ultra-high performance concrete reinforced by glass fibers under accelerated aging, Int. J. Eng. 34 (5) (2021) 1074–1084, https://doi.org/10.5829/IJE.2021.34.05B.01.
- [71] B. Salazar, I. Williams, P. Aghdasi, C. Ostertag, H. Taylor, Bending and crack characteristics of polymer lattice-reinforced mortar, Int. Congr. Polym. Concr. (ICPIC 2018) (2018) 261–266, https://doi.org/10.1007/978-3-319-78175-4 32.
- [72] I. Farina, F. Fabbrocino, G. Carpentieri, M. Modano, A. Amendola, R. Goodall, L. Feo, F. Fraternali, On the reinforcement of cement mortars through 3D printed polymeric and metallic fibers, Compos. Part B: Eng. 90 (2016) 76–85, https://doi. org/10.1016/j.compositesb.2015.12.006.
- [73] Y.J. Nam, Y.K. Hwang, J.W. Park, Y.M. Lim, Feasibility study to control fiber distribution for enhancement of composite properties via three-dimensional printing, Mech. Adv. Mater. Struct. 26 (5) (2019) 465–469, https://doi.org/ 10.1080/15376494.2018.1432809.